1-2018

cGAS Drives Noncanonical-Inflammasome Activation in Age-Related Macular Degeneration

Nagaraj Kerur
University of Kentucky, nagaraj.kerur@uky.edu

Shinichi Fukuda
University of Virginia

Daipayan Banerjee
University of Kentucky, daipayan.banerjee@gmail.com

Younghee Kim
University of Kentucky, young-hee.kim@uky.edu

Dongxu Fu
University of Virginia

See next page for additional authors

Repository Citation

Kerur, Nagaraj; Fukuda, Shinichi; Banerjee, Daipayan; Kim, Younghee; Fu, Dongxu; Apicella, Ivana; Varshney, Akhil; Yasuma, Reo; Fowler, Benjamin J.; Baghdasaryan, Elmira; Marion, Kenneth M.; Huang, Xiwen; Yasuma, Tetsuhiro; Hirano, Yoshio; Serbulea, Vlad; Ambati, Meenakshi; Ambati, Vidya L.; Kajiwara, Yuji; Ambati, Kameshwari; Hirahara, Shuichiro; Bastos-Carvalho, Ana; Ogura, Yuichiro; Terasaki, Hiroko; Oshika, Tetsuro; Kim, Kyung Bo; Hinton, David R.; Leitinger, Norbert; Cambier, John C.; Buxbaum, Joseph D.; Kenney, M. Cristina; Gelfand, Bradley D.; and Ambati, Jayakrishna, "cGAS Drives Noncanonical-Inflammasome Activation in Age-Related Macular Degeneration" (2018). *Ophthalmology and Visual Science Faculty Publications*. 13.
https://uknowledge.uky.edu/ophthalmology_facpub/13

cGAS Drives Noncanonical-Inflammasome Activation in Age-Related Macular Degeneration

Digital Object Identifier (DOI)

https://doi.org/10.1038/nm.4450

Notes/Citation Information

Published in *Nature Medicine*, v. 24, issue 1, p. 50-61.

This is a post-peer-review, pre-copyedit version of an article published in *Nature Medicine.* The final authenticated version is available online at: https://doi.org/10.1038/nm.4450

Authors

Nagaraj Kerur, Shinichi Fukuda, Daipayan Banerjee, Younghee Kim, Dongxu Fu, Ivana Apicella, Akhil Varshney, Reo Yasuma, Benjamin J. Fowler, Elmira Baghdasaryan, Kenneth M. Marion, Xiwen Huang, Tetsuhiro Yasuma, Yoshio Hirano, Vlad Serbulea, Meenakshi Ambati, Vidya L. Ambati, Yuji Kajiwara, Kameshwari Ambati, Shuichiro Hirahara, Ana Bastos-Carvalho, Yuichiro Ogura, Hiroko Terasaki, Tetsuro Oshika, Kyung Bo Kim, David R. Hinton, Norbert Leitinger, John C. Cambier, Joseph D. Buxbaum, M. Cristina Kenney, Bradley D. Gelfand, and Jayakrishna Ambati

Published in final edited form as:
Nat Med. 2018 January ; 24(1): 50–61. doi:10.1038/nm.4450.

cGAS drives non-canonical inflammasome activation in age-related macular degeneration

Nagaraj Kerur[1,2,7,*], **Shinichi Fukuda**[1,2,8], **Daipayan Banerjee**[1,2,7], **Younghee Kim**[1,2,7], **Dongxu Fu**[1,2], **Ivana Apicella**[1,2], **Akhil Varshney**[1,2], **Reo Yasuma**[1,2,7], **Benjamin J. Fowler**[7], **Elmira Baghdasaryan**[10,11], **Kenneth M. Marion**[10], **Xiwen Huang**[10], **Tetsuhiro Yasuma**[8,12], **Yoshio Hirano**[8,13], **Vlad Serbulea**[3], **Meenakshi Ambati**[14], **Vidya L. Ambati**[14], **Yuji Kajiwara**[15], **Kameshwari Ambati**[1,2,7], **Ana Bastos-Carvalho**[7], **Yuichiro Ogura**[13], **Hiroko Terasaki**[12], **Tetsuro Oshika**[8], **Kyung Bo Kim**[9], **David R. Hinton**[16], **Norbert Leitinger**[3], **John C. Cambier**[17], **Joseph D. Buxbaum**[15], **M. Cristina Kenney**[18], **S. Michal Jazwinski**[19], **Hiroshi Nagai**[20], **Isao Hara**[21], **A. Phillip West**[22], **Katherine A. Fitzgerald**[23], **SriniVas R. Sadda**[10,11], **Bradley D. Gelfand**[1,2,4,7], and **Jayakrishna Ambati**[1,2,5,6,7,*]

[1]Center for Advanced Vision Science, University of Virginia School of Medicine, Charlottesville, Virginia, USA

[2]Department of Ophthalmology, University of Virginia School of Medicine, Charlottesville, Virginia, USA

[3]Department of Pharmacology, University of Virginia School of Medicine, Charlottesville, Virginia, USA

[4]Department of Biomedical Engineering, University of Virginia School of Medicine, Charlottesville, Virginia, USA

[5]Department of Pathology, University of Virginia School of Medicine, Charlottesville, Virginia, USA

[6]Department of Microbiology, Immunology, and Cancer Biology, University of Virginia School of Medicine, Charlottesville, Virginia, USA

[7]Department of Ophthalmology and Visual Sciences, University of Kentucky, Lexington, Kentucky, USA

---

[*]Correspondence should be addressed to: J.A. (ja9qr@virginia.edu) or N.K. (nk8m@virginia.edu).

Competing interests

J.A. is a co-founder of iVeena Holdings, iVeena Pharmaceuticals, iVeena Delivery Systems and Inflammasome Therapeutics, and has been a consultant for Allergan, Biogen, and Olix Pharmaceuticals unrelated to this work. J.A., N.K., B.J.F., and K.A. are named as inventors on patent applications on macular degeneration filed by the University of Kentucky or the University of Virginia.

Author contributions

N.K., S.F., D.B., Y.K., D.F., I.A., A.V., R.Y., B.J.F., E.B, K.M.M., X.H. T.Y., Y.H., V.S., M.A., V.L.A., N.L., K.A., A.B.-C., and B.D.G. performed experiments or analyzed data. Y.K., D.R.H., J.C.C., J.D.B., A.P.W., S.M.J., M.C.K. K.A.F., K.B.K, Y.O, H.T., H.N., I.H. and T.O. provided mice, tissues or reagents. J.A. and N.K. conceived and directed the project, and wrote the paper with assistance from B.J.F., B.D.G., N.L., K.A., and S.R.S. All authors had the opportunity to discuss the results and comment on the manuscript.

Data availability:

The datasets generated during and/or analyzed during the current study are not publicly available due to commercialization of research findings but are available from the corresponding author on reasonable request. A Life Sciences Reporting Summary is available.

[8]Department of Ophthalmology, University of Tsukuba, Ibaraki, Japan

[9]Department of Pharmaceutical Sciences, University of Kentucky, Lexington, Kentucky, USA

[10]Doheny Eye Institute, Los Angeles, Los Angeles, California, USA

[11]Department of Ophthalmology, David Geffen School of Medicine, University of California –Los Angeles, Los Angeles, California, USA

[12]Department of Ophthalmology, Nagoya University Graduate School of Medicine, Nagoya, Japan

[13]Department of Ophthalmology, Nagoya City University Graduate School of Medical Sciences, Nagoya, Japan

[14]Center for Digital Image Evaluation, Charlottesville, Virginia, USA

[15]Department of Psychiatry, Icahn School of Medicine at Mount Sinai, New York, New York, USA

[16]Departments of Pathology and Ophthalmology, USC Roski Eye Institute, Keck School of Medicine of the University of Southern California, Los Angeles, California, USA

[17]Department of Immunology and Microbiology, University of Colorado School of Medicine, Aurora, Colorado, USA

[18]Gavin Herbert Eye Institute, University of California Irvine, Irvine, California, USA

[19]Tulane Center for Aging and Department of Medicine, Tulane University Health Sciences Center, New Orleans, Louisiana, USA

[20]Division of Dermatology, Department of Internal Related, Kobe University Graduate School of Medicine, Chuo-ku, Kobe, Japan

[21]Department of Urology, Wakayama Medical University, 811-1 Kimiidera, Wakayama, Japan

[22]Microbial Pathogenesis and Immunology, Texas A&M University, College Station, Texas, USA

[23]Division of Infectious Diseases and Immunology, Department of Medicine, University of Massachusetts Medical School, Worcester, Massachusetts, USA

Abstract

Geographic atrophy is a blinding form of age-related macular degeneration characterized by death of the retinal pigmented epithelium (RPE). In this disease, the RPE displays evidence of DICER1 deficiency, resultant accumulation of endogenous *Alu* retroelement RNA, and NLRP3 inflammasome activation. How the inflammasome is activated in this untreatable disease is largely unknown. Here we demonstrate that RPE degeneration in human cell culture and in mouse models is driven by a non-canonical inflammasome pathway that results in activation of caspase-4 (caspase-11 in mice) and caspase-1, and requires cyclic GMP-AMP synthase (cGAS)-dependent interferon-β (IFN-β) production and gasdermin D-dependent interleukin-18 (IL-18) secretion. Reduction of DICER1 levelsor accumulation of *Alu* RNA triggers cytosolic escape of mitochondrial DNA, which engages cGAS. Moreover, caspase-4, gasdermin D, IFN-β, and cGAS levels are elevated in the RPE of human eyes with geographic atrophy. Collectively, these data highlight an unexpected role for cGAS in responding to mobile element transcripts, reveal cGAS-driven interferon signaling as a conduit for mitochondrial damage-induced inflammasome activation, expand the immune sensing repertoire of cGAS and caspase-4 to non-infectious human disease, and identify new potential targets for treatment of a major cause of blindness.

Age-related macular degeneration affects over 180 million people[1], and is the leading cause of blindness among the elderly across the world. Degeneration of the retinal pigmented epithelium (RPE), a monolayer of cells that provide trophic support to photoreceptors[2,3], is the hallmark of geographic atrophy. the RNase DICER1 are reduced in the RPE of human eyes with geographic atrophy, leading to accumulation of toxic mobile element *Alu* RNA transcripts[4]; these *Alu* transcripts induce RPE cell death by activating the NLRP3 inflammasome[5]. Although NLRP3 inflammasome activation has been widely implicated in macular degeneration[6–8], the mechanisms regulating the inflammasome in this disease remain elusive. Here we demonstrate that DICER1 deficit/*Alu* RNA-driven RPE degeneration in mouse models of macular degeneration is mediated by caspase-4- and gasdermin D-dependent inflammasome activation. Surprisingly this non-canonical inflammasome is dependent on the activation of cyclic GMP-AMP synthase (cGAS)-driven type I interferon signaling (IFN) by cytosolic mitochondrial DNA (mtDNA).

RESULTS

Caspase-4 is activated in AMD

Caspase-4 (caspase-11 is the corresponding mouse protein), which governs non-canonical inflammasome activation, was recently implicated in the immune response to exogenous pathogen-associated molecular patterns (PAMPs) such as intracellular LPS[9,10] and endogenously produced oxidized phospholipids (oxPAPC)[11]. Caspase-4 abundance in the RPE and choroid of human eyes with geographic atrophy was significantly increased compared to normal human eyes from aged subjects, as monitored by western blotting (Fig. 1a and Supplementary Fig. 1a). Introduction of *in vitro* transcribed *Alu* RNA or plasmid-mediated enforced expression of *Alu* RNA (pAlu) induced and activated caspase-4 in primary human RPE cells, as evident by increased abundance of the p30 cleavage fragments (Fig. 1b and Supplementary Fig. 1b, c). Anti-sense oligonucleotide-mediated knockdown of DICER1 similarly induced caspase-4 activation in human RPE cells (Fig. 1b), which was blocked by concomitant anti-sense mediated inhibition of *Alu* RNA (Supplementary Fig. 1d). Caspase-11 activation was induced by subretinal injection of *Alu* RNA in wild-type (WT) C57BL/6J mice (Fig. 1c), and by *Alu* RNA transfection in primary RPE cells isolated from WT mice (Supplementary Fig. 1e). Collectively, these data identify caspase-4 as preferentially activated in human AMD, and indicate that dysregulation of DICER1 and *Alu* RNA lead to caspase-4 activation in this condition.

Caspase-4 is required for *Alu* RNA-induced RPE degeneration and inflammasome activation

We sought to determine whether caspase-4 is required for *Alu* RNA-induced RPE degeneration, which was quantified both by binary grading and semi-automated cellular morphometry (Online Methods and Supplementary Fig. 3).

Exogenous delivery or endogenous over-expression of *Alu* RNA induced RPE degeneration in WT mice (Fig. 1d and Supplementary Fig. 1f). In contrast, subretinal injection of neither *Alu* RNA nor pAlu induced RPE degeneration in *Casp11*$^{-/-}$ mice (Fig. 1d and Supplementary Fig. 1f). 129S6 mice, which lack functional caspase-11 due to a passenger mutation[12], also were resistant to RPE degeneration induced by *Alu* RNA or pAlu (Supplementary Fig. 1g). Subretinal delivery of a cell-permeable, non-immunogenic 17+2-nt cholesterol-conjugated siRNA[13,14] targeting *Dicer1* induced RPE degeneration in WT but not 129S6 mice (Supplementary Fig. 1h). Transgenic expression of human caspase-4 in caspase-11 deficient mice (*Casp11*$^{-/-}$ *hCASP4*^{TG})[15] restored susceptibility to *Alu* RNA-induced RPE degeneration (Fig. 1e), demonstrating that human caspase-4 can compensate for mouse caspase-11 in this system. Collectively, these data demonstrate the critical role of caspase-4 (or mouse caspase-11) in responding to pathological accumulation of endogenous *Alu* mobile element transcripts.

Previously we reported that *Alu* RNA does not induce RPE degeneration in caspase-1 deficient mice[5]. However, this *Casp1*$^{-/-}$ strain was subsequently reported to also lack functional caspase-11 as a result of a passenger mutation in the 129S6 genetic background of this strain[12]; thus, the genotype of these mice is properly referred to as *Casp1*$^{-/-}$ *Casp11*$^{129mt/129mt}$. We sought to clarify the molecular hierarchy of caspases-1 and 11 in response to *Alu* RNA. Whereas *Alu* RNA treatment induced caspase-1 activation in WT mice or RPE cells, *Alu* RNA failed to stimulate caspase-1 activation in *Casp11*$^{-/-}$ mice (Fig. 1f), or in primary RPE cells isolated from *Casp11*$^{-/-}$ mice (Fig. 1g). Reconstitution of caspase-11 into *Casp11*$^{-/-}$ mouse RPE cells restored caspase-1 activation by *Alu* RNA (Supplementary Fig. 2a, b). Moreover, *Alu* RNA failed to induce IL-18 secretion in *Casp11*$^{-/-}$ mouse RPE cells (Fig. 1h). In contrast, caspase-11 was dispensable for IL-18 secretion induced by the canonical inflammasome agonist monosodium urate (MSU) crystals (Supplementary Fig. 10d). These data suggest that caspase-11 is required for caspase-1 activation and IL-18 secretion induced by *Alu* RNA.

Alu RNA did not induce RPE degeneration in *Casp1*$^{-/-}$ *Casp11*$^{129mt/129mt}$ *Casp11*^{Tg} mice[12], in which mouse caspase-11 was functionally reconstituted by a bacterial artificial chromosome transgene (Fig. 1i and Supplementary Fig. 2c. Additionally, as previously observed[5], *Casp1*$^{-/-}$ *Casp11*$^{129mt/129mt}$ mice were not susceptible to *Alu*-induced RPE degeneration (Fig. 1i and Supplementary Fig. 2c), suggesting that both caspase-4/11 and caspase-1 are required for *Alu* toxicity.

Given that we previously demonstrated that PYCARD, an adaptor protein involved in inflammasome activation, and the purinoceptor P2X7 (encoded by *P2rx7*) are required for *Alu* toxicity[5,16,17], we next assessed whether PYCARD and P2X7 are also required for *Alu* RNA-induced caspase-11 activation. *Alu* RNA-induced activation of caspase-11 was reduced in *P2rx7*$^{-/-}$ but not *Pycard*$^{-/-}$ mouse RPE cells, suggesting that caspase-11 is mechanistically positioned between these signaling molecules (Supplementary Fig. 2d, e). Collectively these findings support a model of non-canonical inflammasome activation by *Alu* RNA wherein caspase-4/11 lies upstream of caspase-1 activation.

Recent studies have implicated an endogenous lipid molecule, oxidized phospholipid oxPAPC (oxidized 1-palmitoyl-2-arachidonyl-sn-glycero-3-phosphocholine), in caspase-11-mediated non-canonical NLRP3 inflammasome activation[11]. To test whether *Alu* RNA promotes accumulation of this type of endogenous ligand, we extracted lipids from *Alu* RNA-treated human RPE cells and used liquid chromatography-mass spectrometry to quantify the following products of 1-palmitoyl-2-arachidonoyl-3-phosphatidylcholine (PAPC): 1-palmitoyl-2-glutaryl-3-phosphatidylcholine (PGPC), 1-palmitoyl-2-(5-oxovaleryl)-3-phosphatidylcholine (POVPC), and 1-palmitoyl-2-hydroxy-3-phosphatidylcholine (LysoPC) (Supplementary Fig. 4a-c). Compared to control cells, *Alu* RNA-treated human RPE cells exhibited a two-fold increase in oxPAPC- PGPC and LysoPC levels (Supplementary Fig. 4d), concomitantly with a trend towards a reduction in precursor PAPC levels (Supplementary Fig. 4d). These results suggest an indirect mechanism of *Alu*-driven caspase-11 engagement, possibly via oxidized phospholipid-derived damage-associated molecular patterns (DAMPs).

Gasdermin D is required for *Alu* RNA-induced RPE degeneration and inflammasome activation

Caspase-11-and caspase-1-dependent pyroptotic cell death can be executed by a pore-forming protein, gasdermin D (encoded by *Gsdmd*)[18–20]. We found that *Gsdmd*$^{-/-}$ mice were resistant to *Alu* RNA-induced RPE degeneration (Fig. 2a and Supplementary Fig. 5a, b). Consistent with the role of gasdermin D in non-canonical inflammasome activation by intracellular LPS[19], *Alu* RNA-induced caspase-1 activation and IL-18 secretion were reduced in *Gsdmd*$^{-/-}$ mouse RPE cells (Fig. 2b, c). However, caspase-11 activation in *Gsdmd*$^{-/-}$ mice was not impaired (Fig. 2d), suggesting that loss of caspase-1 activation in *Gsdmd*$^{-/-}$ mouse RPE cells is not due to an indirect effect of gasdermin D on caspase-11, and that, mechanistically, caspase-11 lies upstream of gasdermin D.

Execution of pyroptosis by gasdermin D requires its cleavage into a pore-forming p30 fragment[21]. Interestingly, although gasdermin D was required for *Alu* RNA-induced RPE degeneration and IL-18 secretion, we did not observe its cleavage into a p30 fragment in *Alu* RNA-treated RPE cells in cell culture or in RPE cells *in vivo* (Fig. 2e); however, as reported[19] previously[19], intracellular LPS induced p30 cleavage in mouse bone marrow derived macrophages (BMDMs) (Fig. 2e).

Next, we directly tested whether gasdermin D p30 cleavage is dispensable for the toxicity of *Alu* RNA by reconstituting *Gsdmd*$^{-/-}$ mice with WT gasdermin D (pGSDMD-WT) or mutant gasdermin D (pGSDMD-D276A); pGSDMD-D276A is unable to undergo cleavage into the pyroptotic p30 fragment[19]. Notably, expression of either WT or mutant gasdermin D in *Gsdmd*$^{-/-}$ mice restored susceptibility to *Alu* RNA-induced RPE degeneration (Fig. 2f), suggesting a non-pyroptotic function for gasdermin D in this system.

Previously we demonstrated that *Alu* RNA induces activation of caspase-3 (refs. [4,22]), as well as activation of caspase-8, Fas, and FasL[22], and that this well-characterized pathway of apoptotic induction is critical for the RPE toxicity of *Alu* RNA. In addition, we and others have provided molecular evidence consistent with apoptosis in the RPE in human eyes with geographic atrophy[4,23]. To further clarify the role of apoptosis in *Alu* RNA-induced cell death, we performed live-cell imaging of annexin-V and propidium iodide (PI) staining in primary human RPE cells. Cells treated with *Alu* RNA developed plasma membrane blebs and displayed an annexin-V^+ PI^- staining pattern, findings that are consistent with early apoptosis. After several hours of annexin-V positivity, cells frequently swelled and became PI–positive, consistent with late apoptosis or secondary necrosis[24] (Supplementary Fig. 6a, b). *In vivo* studies recapitulated these cell culture findings: RPE flat mounts from *Alu* RNA-exposed WT mice displayed predominantly annexin-V^+ PI^- cell death (Supplementary Fig. 7a). *Alu* RNA treatment of RPE cells induced cleavage of caspase-3 and poly(ADP-ribose) polymerase 1 (PARP-1) (Supplementary Fig. 7b), further supporting induction of an apoptotic cell death pathway. These findings, coupled with our earlier demonstration that neither necrostatin-1, an inhibitor of primary necrosis, nor glycine, an inhibitor of pyroptosis[25], blocks *lu* RNA-induced RPE degeneration[5,22], suggest that *Alu* RNA promotes cell death primarily via apoptosis rather than pyroptosis or necrosis in RPE cells.

Next, we explored the roles of IL-18 and gasdermin D in *Alu* RNA-induced cell death. The resistance of *Gsdmd*$^{-/-}$ mice to *Alu* RNA-induced RPE degeneration was overcome by recombinant mature IL-18 or subretinal injection of a plasmid expressing mature IL-18, suggesting that this resistance is due to loss of IL-18 secretion (Fig. 2g). Supportive of this concept, *Alu* RNA failed to induce secretion of IL-18 in *Gsdmd*$^{-/-}$ mouse RPE cells, and this effect was rescued by reconstitution of the cells with either pGSDMD-WT or the p30 cleavage-incompetent pGSDMD-D276A (Supplementary Fig. 5c). Additionally, whereas annexin-V^+ cells were not visible in RPE flat mounts of *Alu* RNA-treated *Gsdmd*$^{-/-}$ mice, administration of recombinant mature IL-18 led to the appearance of numerous annexin-V^+ PI^- cells (Supplementary Fig. 8). Taken together with our previous demonstration that IL-18 neutralization or IL-18 receptor deficiency in mice blocks *Alu* RNA toxicity *in vivo*[5], these findings suggest that gasdermin D is required for *Alu* RNA-induced inflammasome activation, and for RPE toxicity driven via IL-18-dependent apoptosis.

Gasdermin D mRNA abundance was elevated in the RPE of human eyes with geographic atrophy, as compared to eyes from unaffected age-matched controls (Fig. 2h). In contrast, we observed similar levels of MIP-1α, IL-8, and IL-6 mRNA in geographic atrophy and normal specimens (Supplementary Fig. 5d), suggesting that global elevation of pro-inflammatory cytokines does not occur in GA, but rather a more specific increase in the expression of inflammasome pathway genes. We also observed increased gasdermin D protein expression in the RPE of human eyes with geographic atrophy, as compared to eyes from unaffected age-matched controls (Fig. 2i).

Alu RNA-induced non-canonical inflammasome activation is driven by Type I interferon (IFN) signaling

To interrogate the upstream regulation of caspase-4, we focused on interferon signaling, which is involved in activation of the caspase-11 driven non-canonical inflammasome[10]. *Alu* RNA did not induce RPE degeneration or caspase-11 activation in *Ifnar1*$^{-/-}$ mice or *Ifnar1*$^{-/-}$ mouse RPE cells (Fig. 3a, b), which are deficient in the type I interferon-α/β receptor (IFNAR). Treatment with recombinant interferon-β increased caspase-4 abundance in human RPE cells (Fig. 3c). *Alu* RNA induced secretion of interferon-β (Fig. 3d) and phosphorylation of IRF3 (Supplementary Fig. 9a), a transcription factor that induces production of interferon-β. *Alu* RNA also induced phosphorylation of STAT2 (Fig. 3e and Supplementary Fig. 9a, b), a signaling molecule activated by type-I interferons downstream of IFNAR. *Alu* RNA-induced RPE degeneration was blocked by administration of an IFN-β neutralizing antibody (Fig. 3f). Moreover, *Alu* RNA did not induce RPE degeneration in *Irf3*$^{-/-}$ or *Stat2*$^{-/-}$ mice (Fig. 3g, and Supplementary Fig. 9c, d), and induction of caspase-11 activation by *Alu* RNA was reduced in *Stat2*$^{-/-}$ mouse RPE cells (Supplementary Fig. 9e). Human eyes with geographic atrophy displayed pronounced IFN-β expression in the RPE, as compared to eyes from unaffected age-matched controls (Fig. 3h, i). Taken together, these data suggest that *Alu* RNA-induced RPE degeneration is dependent on regulation of the non-canonical inflammasome by type I interferon signaling.

cGAS-driven IFN signaling licenses non-canonical NLRP3 inflammasome

We sought to identify the upstream activator of IRF3-driven interferon signaling induced by *Alu* RNA. We previously showed that *Alu* RNA-induced RPE degeneration is independent of several IRF3-activating signaling molecules, including various RNA sensors: TLR3, TLR4, TLR9, RIG-I, MDA5, MAVS, and TRIF[5]. Cyclic GMP-AMP synthase (cGAS, encoded by *Mb21d1*) has emerged as an innate immune sensor that can activate type I interferon signaling[26]. Additionally, a role for cGAS in broadly inhibiting several RNA viruses has also been reported[27].

We found that *Alu* RNA upregulated cGAS mRNA and protein in human RPE cells (Supplementary Fig. 10a, b). In contrast to WT mouse RPE cells, *Alu* RNA did not induce interferon-β (Fig. 4a), activate caspase-1 (Fig. 4b and Supplementary Fig. 10c) or caspase-11 (Fig. 4c), or induce IL-18 secretion (Fig. 4d) in *Mb21d1*$^{-/-}$ mouse RPE cells. In contrast, inflammasome activation by MSU crystals was unimpaired in *Mb21d1*$^{-/-}$ mouse RPE cells (Supplementary Fig. 10d). In human RPE cells, DICER1 knockdown-induced induction of interferon-β, STAT2 phosphorylation, and activation of caspase-4 and caspase-1, were all inhibited by knockdown of cGAS (Fig. 4e, f and Supplementary Fig. 10e, f). Corroborating these data, *Alu* RNA did not induce RPE degeneration in *Mb21d1*$^{-/-}$ mice (Fig. 4g and Supplementary Fig. 10g, h). Additionally, reconstitution of mouse cGAS restored IFN-β induction in *Mb21d1*$^{-/-}$ mouse RPE cells and RPE degeneration in *Mb21d1*$^{-/-}$ mice (Fig. 4h, Supplementary Fig. 10i, and Supplementary Fig. 11a). Moreover, the resistance of *Mb21d1*$^{-/-}$ mice to *Alu* RNA-induced RPE degeneration was overcome by recombinant IFN-β administration or IFN-β expression via subretinal plasmid transfection (Fig. 4i), suggesting that this resistance is indeed due to lack of IFN signaling.

cGAS protein was more abundant in the RPE of human eyes with geographic atrophy as compared to eyes from unaffected age-matched controls (Fig. 5a). cGAS-driven interferon signaling can be transduced by the adaptor protein STING (encoded by *Tmem173*)[26]. *Alu* RNA did not induce IRF3 phosphorylation (Supplementary Fig. 11b, c) or activation of caspase-1 (Fig. 5b) or caspase-11 (Fig. 5c) in *Tmem173*$^{-/-}$ mouse RPE cells, and did not induce RPE degeneration in *Tmem173*$^{-/-}$ mice (Fig. 5d), pointing to the involvement of the cGAS-STING signaling axis in this system. As in the case of *Mb21d1*$^{-/-}$ mice, the resistance of *Tmem173*$^{-/-}$ mice to *Alu* RNA-induced RPE degeneration was overcome by recombinant IFN-β administration or IFN-β expression via subretinal plasmid transfection (Fig. 5e), which again points to the requirement for IFN signaling in *Alu* RNA-induced RPE degeneration.

Alu-driven cGAS activation is triggered by engagement with mtDNA

cGAS is activated by cytosolic DNA but not by poly(I:C), a synthetic double stranded RNA analog[26]. Consistent with the notion that cGAS does not recognize RNA directly, *Alu* RNA did not bind cGAS in an RNA immunoprecipitation assay (data not shown). Previous studies have implicated mitochondrial dysfunction in macular degeneration, including mitochondrial DNA (mtDNA) damage, reactive oxygen species (ROS) production, and downregulation of proteins involved in mitochondrial energy production and trafficking[5,28,29]. Cytosolic escape of mitochondrial components, such as DNA and formyl peptides, have been shown to activate innate immune pathways, including cGAS (refs. [30]).

Both *Alu* RNA stimulation and DICER1 knockdown in human RPE cells resulted in an increased cytosolic abundance of mtDNA (Fig. 6a and Supplementary Fig. 12a, b). To examine whether *Alu* RNA triggers engagement of mtDNA by cGAS, we performed a DNA-protein interaction pull down assay in *Mb21d1*$^{-/-}$ immortalized mouse embryonic fibroblasts reconstituted with HA-tagged cGAS (ref. [30]). As these cells express HA-cGAS from a genomically integrated DNA sequence, they would be expected to express HA-cGAS at levels similar to those of endogenous cGAS expression. We observed enrichment of mtDNA in cGAS immunoprecipitates of *Alu* RNA-stimulated but not mock- or poly(I:C)-stimulated cells (Fig. 6b and Supplementary Fig. 12c), suggesting that mtDNA in the cytosol engages cGAS. As a positive control, transfected plasmid DNA in this assay was also enriched in the cGAS immunoprecipitate (Supplementary Fig. 12d). Additionally, subretinal delivery of mtDNA induced RPE degeneration in WT but not in *Mb21d1*$^{-/-}$ mice (Supplementary Fig. 12e). Similarly, in cell culture studies, mtDNA-induced *Ifnb* mRNA levels were reduced in *Mb21d1*$^{-/-}$ compared to WT mouse RPE cells (Supplementary Fig. 12f). These data indicate that *Alu* RNA-induced RPE degeneration is mediated via release of mtDNA into the cytosol, where it interacts with cGAS and induces interferon-β expression.

The mitochondrial permeability transition pore is required for *Alu*-driven mtDNA release

During conditions of cellular stress, opening of the mitochondrial permeability transition pore (mPTP) leads to mitochondrial swelling, rupture, and release of mitochondrial contents into the cytosol[31]. In cells lacking mitochondrial peptidyl-prolyl cis-trans isomerase F (PPIF, also known as cyclophilin D), a key enzyme involved in mPTP opening, mitochondria are resistant to swelling and the permeability transition[32]. Using the JC-1 and cobalt-calcein assays, we found that *Alu* RNA induced a reduction of mitochondrial membrane potential ($\Delta\Psi$m), indicative of mPTP opening, in wild-type but not *Ppif*$^{-/-}$ mouse RPE cells, as determined using the potential-sensitive fluorochrome JC-1, and by quenching of the calcein signal (Supplementary Fig. 12g, h). In addition, cyclosporine A, which inhibits mPTP opening via binding to PPIF, blocked *Alu* RNA-induced mPTP opening in wild-type cells, but did not alter $\Delta\Psi$m or calcein signal intensity in *Ppif*$^{-/-}$ cells (Supplementary Fig. 12g, h). Collectively, these findings suggest that *Alu* RNA induces *Ppif*-dependent mPTP opening in RPE cells.

Consistent with an effect of *Alu* RNA on mPTP opening, *Alu* RNA triggered mtDNA release into the cytosol in WT but not *Ppif*$^{-/-}$ mouse RPE cells (Fig. 6c). *Ppif*$^{-/-}$ mice were protected against *Alu* RNA-induced RPE degeneration (Fig. 6d), confirming the *in vivo* importance of mPTP in *Alu* toxicity, and *Alu* RNA-induced activation of caspase-1 and caspase-11 were reduced in *Ppif*$^{-/-}$ mouse RPE cells (Fig. 6e, f). In human RPE cells lacking mitochondrial DNA (Rho^{0} ARPE19 cells), *Alu* RNA no longer activated caspase-4 (Fig. 6g) or induced secretion of IL-18 (Fig. 6h) or IFN-β (Fig. 6i). Furthermore, the resistance of *Ppif*$^{-/-}$ mice to *Alu* RNA-induced RPE degeneration was overcome by recombinant IFN-β administration or IFN-β expression via subretinal plasmid transfection (Fig. 6j). Collectively these data support a model wherein mPTP-driven mitochondrial permeability mediates cytosolic release of mtDNA, which in turn promotes non-canonical inflammasome activation, via engagement of the cytosolic DNA sensor cGAS and its induction of IFN signaling.

Alu driven RPE toxicity does not require macrophages or microglia

We focused on the RPE as the cellular locus of inflammasome activation because we previously demonstrated that the various molecular abnormalities associated with geographic atrophy—DICER1 deficiency, *Alu* RNA accumulation, and increased abundance of NLRP3, PYCARD, cleaved caspase-1, and phosphorylated IRAK1/4—are localized to the RPE layer of human eyes with geographic atrophy[4,5]. Our current observations that elevated levels of cGAS, gasdermin D, cleaved caspase-4, and IFN-β are similarly localized to the RPE layer in diseased eyes buttresses the notion that this cell layer is the locus of molecular perturbations in the non-canonical inflammasome pathway.

However, recent reports that macrophages and microglia can be observed in the vicinity of pathology in human eyes with geographic atrophy[33] raise the question of the functional involvement of these immune cells. Previously we demonstrated that RPE cell-specific ablation of Myd88, the adaptor critical for IL-18-induced RPE cell death in this system, is sufficient to prevent *Alu* RNA-induced RPE degeneration in mice[5]. We also demonstrated using mouse chimeras that ablation of *Myd88* in circulating bone marrow derived cells does not prevent *Alu* RNA-induced RPE degeneration[5]. Nevertheless, given that macrophages and microglia are capable of inflammasome signaling, we studied their involvement more directly. We depleted macrophages using clodronate liposomes[34] and depleted microglia by administering tamoxifen to *Cx3cr1*^{CreER} ROSA-DTA mice[35]. Although these manipulations successfully depleted macrophages and microglia, respectively, neither type of depletion blocked *Alu* RNA- induced RPE degeneration *in vivo*, providing direct evidence that these two cell populations are dispensable for RPE toxicity in this system (Supplementary Fig. 13).

Although these two cell types are apparently not required by *Alu* RNA to elicit RPE degeneration in mice, they might have more subtle effects on disease pathology. Consistent with this possibility, we found that *Alu* RNA activated the non-canonical inflammasome in mouse BMDMs (Supplementary Fig. 14). Similarly to RPE cells, the ability of *Alu* RNA to induce caspase-1 activation was impaired in *Casp11*$^{-/-}$, *Mb21d1*$^{-/-}$, and *Gsdmd*$^{-/-}$ BMDMs, as compared to WT BMDMs (Supplementary Fig. 14). Collectively these findings suggest that cGAS-driven licensing of the non-canonical inflammasome by *Alu* RNA is not restricted to RPE cells.

DISCUSSION

Our data identify an unexpected role for the DNA sensor cGAS, the non-canonical caspase-4 inflammasome, and gasdermin D in mediating *Alu* RNA-induced RPE cell death, both in mice in vivo and in human cell culture. Coupled with observations that cGAS, interferon-β, caspase-4, and gasdermin D are at increased abundance in the RPE of human eyes with geographic atrophy as compared to control unaffected eyes, our findings point to the involvement of these proteins in the pathogenesis of this form of age-related macular degeneration.

cGAS was originally recognized as a sensor of exogenous and endogenous cytosolic DNA that mediates IRF3-driven interferon signaling, and previous studies demonstrated that the enzymatic activity of cGAS could not be activated by an RNA stimulus[26]. Nonetheless, cGAS has been reported to be critical for the antiviral response to multiple RNA viruses[27]; although the mechanistic underpinnings of this effect are not fully understood. In this context, our work provides a new view of how which endogenous RNAs can activate cGAS, and raise the possibility that cGAS-driven antiviral immunity involves *Alu* RNA, whose levels can be stimulated by viral infections[36], leading to mitochondrial dysfunction.

Mitochondria have been increasingly implicated as gatekeepers of cell fate, with decisive roles in diverse cellular responses including apoptosis, autophagy, and innate immunity[37]. Mitochondria can facilitate the innate immune response to infection and injury via release of mitochondrial components that are recognized as DAMPs by the cell's innate immune components. Of note, mtDNA can activate multiple arms of innate immunity, including the NLRP3 inflammasome, TLR9, and cGAS/STING-driven IFN signaling[38,39]. In particular, mtDNA can activate the NLRP3 inflammasome by directly interacting with NLRP3 (ref. [40]) or by amplifying the response to an initial trigger, such as ATP or ROS[41]; and mtDNA can activate TLR9 on neutrophils, triggering systemic lung and liver inflammation[42]. In addition to engaging TLR9 and NLRP3 signaling, mtDNA has also recently been reported to be involved in the activation of cGAS signaling via cytosolic escape of mtDNA as a consequence of mitochondrial stress[30]. We previously demonstrated that TLR9 signaling is dispensable for *Alu* RNA-induced RPE degeneration[5], and that NLRP3 inflammasome priming is unaffected in mouse RPE cells lacking TLR9 (ref. [17]). Instead, our findings show that *Alu* RNA-driven cytosolic mtDNA release leads to activation of both inflammasome and cGAS signaling pathways, highlighting the role of mitochondria as a signaling platform that integrates various cellular stress cues into an innate immune signaling response in autoimmune and chronic inflammatory diseases.

In addition to its role in responding to infections, cGAS has been implicated in mouse models of autoimmune diseases and mouse tumor models. Our findings expand the functional repertoire of this innate immune sensor to chronic degenerative diseases. Caspase-4/11-mediated activation of the non-canonical NLRP3 inflammasome has been implicated in gram-negative bacterial infection, sepsis, and antimicrobial defense at the mucosal surface[10,12]. To our knowledge, our report is the first example of caspase-4-driven non-canonical inflammasome activation in a non-infectious human disease. The involvement of caspase-4 and cGAS in other conditions such as systemic lupus erythematosus and diabetes mellitus, wherein *Alu* RNA accumulation has been observed[43,44], bears future investigation. Activation of caspase-4 has been observed in conditions of endoplasmic reticulum (ER) stress[45]. Given that several human diseases including Alzheimer's disease and obesity driven-type 2 diabetes, both of which are driven by a hyperactive inflammasome, are associated with ER stress[46,47], it would also be worth exploring whether DICER1 deficiency and/or *Alu* RNA-induced mitochondrial dysfunction and cGAS- and caspase-4 dependent-inflammasome activation are linked to ER stress.

Gasdermin D has not, to our knowledge, been shown previously to be involved in a non-infectious human disease. Mechanistically, we found that gasdermin D lies downstream of caspase-11 activation and is required for *Alu* toxicity. The role of gasdermin D in this system appears not to be induction of pyroptosis, as it is in response to exogenous triggers such as intracellular LPS. Instead, gasdermin D supports *Alu* RNA-induced RPE cell apoptosis by promoting IL-18 secretion; notably, we did not observe cleavage of gasdermin into its p30 fragment, a cleavage which is required for its pyroptotic effect. Additional studies are required to dissect the mechanisms that disengage the pore-forming function of gasdermin D from the inflammasome-activating function, i.e., caspase-1 activation and IL-18 secretion. The effects of non-canonical inflammasome-dependent gasdermin D activation might be dictated by the activating trigger (e.g. exogenous versus host) or the cell type. For instance, the only other endogenous molecule known to activate caspase-11, oxPAPC, also does not induce pyroptosis, but instead triggers IL-1β release from dendritic cells[11].

The mechanisms underlying regulation of the NLRP3 inflammasome by caspase-11/4 have been elusive. Previously we demonstrated that *Alu* RNA-induced RPE degeneration and NLRP3 inflammasome activation depend on NF-κB and P2X7 (refs. [16,17]). In our current work, we found that *Alu* RNA-induced caspase-11 activation was subdued in $P2rx7^{-/-}$ mouse RPE cells, suggesting that P2X7 is required for both caspase-1 and caspase-11 activation.[48] Taken together, our observations suggest that *Alu* RNA-driven NLRP3 inflammasome activation requires both caspase-11/4 and P2X7 We also observed that *Alu* RNA induces oxPAPC synthesis, suggesting that *Alu* RNA might recruit other DAMPs to activate the non-canonical inflammasome and cause RPE cell toxicity. Earlier reports have implicated oxidized phospholipids in the pathophysiology of age-related macular degeneration[49,50]; future studies to unravel the underlying molecular mechanisms should be performed.

In recent years, numerous groups employing a variety of cell culture systems, animal models, and human donor eyes have reported an important role for the inflammasome in AMD[5–8,51–54]. Collectively these studies suggest that NLRP3 pathway is an important responder to a panoply of AMD-related molecular stressors and toxins in RPE cells, and there is great interest in inflammasome inhibition as a therapeutic for AMD[16]. Our identification of cGAS, interferon-β, caspase-4, and gasdermin D as critical mediators in inflammasome-driven RPE degeneration expands the array of therapeutic targets for AMD.

Although there is consensus that NLRP3 inflammasome activation is detrimental to RPE cell health and survival[6–8], akin to the effects of NLRP3 inflammasome activation in other cell types[55,56], there is controversy about the role of this pathway in neovascular AMD. It has been reported that IL-18, a cytokine produced by NLRP3 inflammasome activation, inhibits angiogenesis and that IL-18 neutralization augments angiogenesis in a laser injury model of choroidal neovascularization[54]. However, we and others were unable to replicate this anti-angiogenic effect of IL-18, and it was also demonstrated that the promotion of angiogenesis by an IL-18 antibody is due to an excipient in its preparation[57]. These conflicting data in neovascular AMD models do not, however, bear on the conclusion from our current data and work by others that inflammasome activation promotes RPE degeneration, a concept that provides a mechanistic rationale for testing inflammasome inhibition in geographic atrophy[57,4,58,59,3,60]

In summary, this study has uncovered a contribution of endogenous retroelement transcripts to disease via its induction of mitochondrial dysfunction and cGAS signaling, which drives interferon signaling and gasdermin D and NLRP3 inflammasome activation (Supplementary Fig. 15). Targeting of this pathway provides a new potential therapeutic approach for preserving RPE health in age-related macular degeneration and for treatment of a host of other inflammasome-driven diseases.

Methods

Mice

All animal experiments were approved by University of Kentucky's or University of Virginia's institutional review committees and were performed in accordance with the Association for Research in Vision and Ophthalmology Statement for the Use of Animals in Ophthalmic and Visual Research. Both male and female mice between 6–10 weeks of age were used in the study. Wild-type C57BL/6J, *Ppif*$^{-/-}$, *P2rx7*$^{-/-}$ and *Stat2*$^{-/-}$ mice were purchased from The Jackson Laboratory. *Gsdmd*$^{-/-}$, *Pycard*$^{-/-}$, *Casp11*$^{-/-}$, *Casp1*$^{-/-}$ Casp11$^{129mt/129mt}$ and *Casp1*$^{-/-}$ *Casp11*$^{129mt/129mt}$ *Casp11*$^{\mathrm{Tg}}$ mice, described elsewhere[12,19,61,62], were a generous gift from V.M Dixit (Genentech). Caspase-11 deficient mouse transgenically expressing human caspase-4 (*Casp11*$^{-/-}$ *hCasp4*^{Tg}) were described earlier[15]. Wild type 129S6 mice (that carry an inactivating passenger mutation in caspase-11) were purchased from Taconic Biosciences. *Ifnar1*$^{-/-}$ mice were described earlier[63] and were a generous gift from M. Aguet. *Irf3*$^{-/-}$ mice were a generous gift from T. Taniguchi via M. David[64]. *Mb21d1*$^{-/-}$ mice were generated by K.A. Fitzgerald (University of Massachusetts Medical School) on a C57BL/6 background using cryopreserved embryos obtained from the European Conditional Mouse Mutagenesis Program (EUCOMM)[65]. *Tmem173*$^{-/-}$ mice were described earlier[66]. For all procedures, anesthesia was achieved by intraperitoneal injection of 100 mg/kg ketamine hydrochloride (Ft. Dodge Animal Health) and 10 mg/kg xylazine (Phoenix Scientific), and pupils were dilated with topical 1% tropicamide and 2.5% phenylephrine (Alcon Laboratories).

Fundus Photography

A TRC-50 IX camera (Topcon) linked to a digital imaging system (Sony) was used for fundus photographs of dilated mouse eyes.

Subretinal Injection

Subretinal injections (1 μl) in mice were performed using a Pico-Injector (PLI-100, Harvard Apparatus) or using a 35-gauge needle (Ito Co. Fuji, Japan). *In vivo* transfection of plasmids expressing *Alu* sequences (pAlu)[67,68], empty control vector (pNull), Flag-cGAS (pFlag-cGAS), Flag-GFP, mouse mature IL-18 (pIL-18ss)[57,69], wildtype mouse gasdermin D (pGSDMD-WT), the p30 cleavage incompetent mutant mouse gasdermin D ((pGSMDD-D276A)[19], IFN-β (Origene Cat# MR226101), or mtDNA (10 ng) was achieved using 10% Neuroporter (Genlantis) as previously described[4,5]. *In vitro* transcribed *Alu* RNA (0.15–0.3 μg/μl), IFN-β neutralizing antibody (10 ng; Abcam Cat# ab24324), control isotype IgG, recombinant IL-18 (100 ng/μl, MBL Cat#B002-5), or IFN-β (500 mUnit/μl, PBL Cat#12410-1) were administered via subretinal injection[4,5]. Similarly, to knock down *Dicer1*, 1 μl of cholesterol conjugated siRNA (1 μg/μl) targeting mouse *Dicer1* or scrambled control siRNAs were injected (Dicer1 siRNA sense- CUCUGUGAGAGUUGUCCdTdT; Control siRNA sense- UAAGGCUAUGAAGAGAUdTdT). The eye used for active versus control injection was chosen randomly.

Assessment of RPE Degeneration

Alu-mediated RPE degeneration was induced by exposing mice to *Alu* RNA, as previously described[4,5,16,17,22]. Seven days later, RPE health was assessed by fundus photography and immunofluorescence staining of zonula occludens-1 (ZO-1) on RPE flat mounts (whole mount of posterior eye cup containing RPE and choroid layers). Mouse RPE and choroid flat mounts were fixed with 4% paraformaldehyde or 100% methanol, stained with rabbit polyclonal antibodies against mouse ZO-1 (1:100, Invitrogen) and visualized with Alexa-594 (Invitrogen). All images were obtained by microscopy (model SP-5, Leica; or Axio Observer Z1, Zeiss). Imaging was performed by an operator masked to the group assignments.

Quantification of RPE Degeneration

Binary Assignment—Healthy RPE cells form a polygonal tessellation with a principally hexagonal “honeycomb” formation. RPE degeneration was assessed as a disruption of this uniformity of this polygonal sheet. Thus, RPE health was assessed as the presence or absence of morphological disruption in RPE flat mounts by two independent raters who were masked to the group assignments. Both raters deemed 100% of images as gradeable. Inter-rater reliability was measured by agreement on assignments, Pearson coefficient of determination, and Fleiss κ. Fisher’s exact test was used to determine statistical significance between the fraction of healthy RPE sheets across groups.

Cellular Morphometry—Quantification of cellular morphometry for hexagonally packed cells was performed in semi-automated fashion by three masked graders by adapting our previous analysis of corneal endothelial cell density[70]. As RPE cells when viewed *en face* typically exhibit a principally hexagonal morphology similar to the corneal endothelium, they readily lend themselves to a similar analysis strategy. We obtained measures of cell size, polymegethism (coefficient of variation of cell size), and cell density. For this analysis, microscopy images of the RPE were captured and transmitted in deidentified fashion to the Doheny Image Reading & Research Lab (DIRRL). Images in which no cell borders could be seen were excluded from further analysis (1.8%). All images were rescaled to 304 × 446 pixels to permit importation into the Konan CellCheck software (Ver. 4.0.1), a commercial U.S. FDA-cleared software that has been used for registration clinical trials. RPE cell metrics were generated by three certified reading center graders in an independent, masked fashion. Inter-grader agreement was assessed for all three metrics by computing the multiple adjusted coefficient of determination. The previously published center method was utilized which entails the user selecting the center of each identifiable cell in the image[71–74]. Once the cell centers were defined, the software automatically generated the mean cell area, cell density, and polymegethism values. By default, the Konan software assumes a scaling factor of 124 pixels per 100 μm. Based on the dimensions of the original RPE image (1,024 × 1,024 pixels, 0.21 μm/pixel), the Konan provided values were converted to the actual physical values in μm.

RPE degeneration was quantified based on zonula occludens (ZO)-1-stained flat mount images using two strategies:

1. Binary assignment (healthy versus unhealthy)[16,17,22] by two masked raters (inter-rater agreement = 98.6%; Pearson $r^2 = 0.95$, $P < 0.0001$; Fleiss $\kappa = 0.97$, $P < 0.0001$).
2. Semi-automated cellular morphometry analysis by three masked raters adapting our prior analysis of the planar architecture of the corneal endothelium[70], which resembles the RPE in its polygonal tessellation. Inter-rater agreement was high for all three metrics (multiple adjusted $r^2 = 0.99$ (cell size), 0.72 (polymegethism, i.e., coefficient of variation of cell size), 0.99 (cell density)).

For eyes treated with *Alu* RNA, pAlu, and their respective controls, inter-rater agreement on binary assignment was 100%, and the fraction of eyes classified as healthy was 100% for both control groups versus 0% for *Alu* RNA or pAlu treatments ($P < 0.0001$, for both comparisons, Fisher exact test). All three morphometric features were significantly different between control treatments versus *Alu* RNA or pAlu treatments ($P < 0.0001$, t test; Supplementary Fig. 3). Given the similarity among all three features in differentiating healthy versus degenerated RPE cells, for all remaining groups, we quantified polymegethism, a prominent geometric feature of RPE cells in human geographic atrophy[4,75–77].

Human Tissue

All studies on human tissue followed the guidelines of the Declaration of Helsinki. The study of deidentified tissue from deceased individuals obtained from various eye banks in the United States was exempted from IRB review by the University of Virginia Institutional Review Board for Health Sciences Research in accordance with U.S. Health & Human Services human subjects regulations. Donor eyes from patients with geographic atrophy, an advanced form of AMD or age-matched patients without AMD were obtained from various eye banks. These diagnoses were confirmed by dilated ophthalmic examination prior to acquisition of the tissues or eyes or upon examination of the eye globes post mortem. Enucleated donor eyes isolated within six hours post mortem were immediately preserved in RNALater (ThermoFisher). The neural retina was removed and tissue comprising both macular RPE and choroidal tissue were snap frozen in liquid nitrogen. For eyes with GA, RPE and choroidal tissue comprising both atrophic and marginal areas were collected.

Immunohistochemistry

Human eyes fixed in 2–4% paraformaldehyde were prepared for immunohistochemistry and stained as described earlier[4,5]. Briefly, immunohistochemical staining of fixed human eyes was performed with rabbit antibody against cGAS (0.1 µg/ml, Sigma-Aldrich, Cat# HPA031700) or interferon β (0.2 µg/ml, Santa Cruz Biotechnology, Cat# sc-20107) and mouse antibody against gasdermin D (1.5 µg/ml, Abcam, Cat# ab57785). Rabbit or mouse IgG controls were used to ascertain the specificity of the staining. Biotin-conjugated secondary antibodies, followed by incubation with VECTASTAIN® ABC reagent and development using Vector Blue (Vector Laboratories), were utilized to detect the bound primary antibody. Slides were washed in PBS, and then mounted in Vectamount (Vector Laboratories). All images were obtained using a Zeiss Axio Observer Z1 microscope.

Real-time PCR

Total RNA purified from cell using Trizol reagent (Invitrogen) following the manufacturer’s recommendations was DNase treated and reverse transcribed using the QuantiTect® Reverse Transcription kit (QIAGEN). The RT products (cDNA) were amplified by real-time quantitative PCR (Applied Biosystems 7900 HT Fast Real-Time PCR system) with Power SYBR green Master Mix. Relative gene expression was determined by the $2^{-\Delta\Delta Ct}$ method using 18S rRNA or GAPDH as an internal control. The primers used were as follows: human IFNB1 (forward 5′-GCGACACTGTTCGTGTTGTC-3′ and reverse 5′-GCCTCCCATTCAATTGCCAC-3′), human CASP4 (forward 5′-TCTGAGGCTCTTTCCAACGC-3′ and reverse 5′-TTTGCCCAGGGATTCCAACA-3′), human DICER (forward 5′ AGAGGGAAAGAAAGACAACTGCT-3′ and reverse 5′-CATGCTGAGGGGTTGCAAAG-3′), human cGAS (forward 5′-ACGTGCTGTGAAAACAAAGAAG-3′ and reverse 5′-GTCCCACTGACTGTCTTGAGG-3′), human 18s rRNA (forward 5′-CGCAGCTAGGAATAATGGAATAGG-3′and reverse 5′-GCCTCAGTTCCGAAAACCAA-3′), human mitochondrial DNA (forward 5′-AGCCCACTGTAAAGCTAA-3′ and reverse 5′-TGGGTGATGAGGAATAGTGTA-3′), human GAPDH (forward 5′-TGGAAATCCCATCACCATCT-3′ and reverse 5′GTCTTCTGGGTGGCAGTGAT-3′), human GSDMD (forward 5′-GCTCCATGAGAGGCACCTG-3′ and reverse 5′-TTCTGTGTCTGCAGCACCTC-3′) mouse Ifnb1 (forward 5′-CGTGGGAGATGTCCTCAACT-3′ and reverse 5′-CCTGAAGATCTCTGCTCGGAC-3′), mouse Gapdh (forward 5′-CGACTTCAACAGCAACTCCCACTCTTCC-3′ and reverse: 5′-TGGGTGGTCCAGGGTTTCTTACTCCTT-3′), mouse 18s rRNA (forward 5′-TTCGTATTGCGCCGCTAGA-3′ and reverse 5′- CTTTCGCTCTGGTCCGTCTT-3′), mouse mitochondrial DNA (forward 5′-TTCGGAGCCTGAGCGGGAAT-3′ and reverse 5′-ATGCCTGCGGCTAGCACTGG-3′). human MIP1α (forward 5′-CATCACTTGCTGCTGACACG-3′ and reverse 5′-TGTGGAATCTGCCGGGAG-3′), human IL6 (forward 5′-GTAGCCGCCCCACACAGA-3′ and reverse 5′-CATGTCTCCTTTCTCAGGGCTG-3′), human IL8 (forward 5′-CACCGGAAGGAACCATCTCA-3′ and reverse 5′-AGAGCCACGGCCAGCTT-3′).

Mitochondrial DNA Preparation

Total DNA extracted from ARPE19 cells was used to PCR-amplify mtDNA segments as described earlier[78]. The purified mtDNA PCR products were subretinally delivered using 10% Neuroporter (Genlantis) as described above.

Western Blotting

Cell and tissue lysates prepared in RIPA buffer where homogenized by sonication. Protein concentration was determined using the Pierce BCA Protein Assay Kit (Thermo Fisher Scientific Inc.). Equal quantities of protein (10–50 μg) prepared in Laemmli buffer were resolved by SDS-PAGE on Novex® Tris-Glycine Gels (Invitrogen) and transferred onto Immobilon-FL PVDF membranes (Millipore). The transferred membranes were blocked in Odyssey® Blocking Buffer (PBS) or 5% nonfat dry skim milk for 1 h at RT and then incubated with primary antibody at 4 °C overnight. The immunoreactive bands were visualized using species specific secondary antibodies conjugated with IRDye® or HRP. Blot images were either captured using an Odyssey® imaging system or autoradiography film. The antibodies used were as follows; rabbit polyclonal anti-human and mouse caspase-1 antibodies (1:500, Biovision Cat# 3019-100; 1:1000, Invitrogen Cat#AHZ0082; 1:200 Santa Cruz Biotechnology Cat#sc-514), rabbit anti-caspase-1 mAb (1:1000, Abcam Cat# ab108362), anti-human caspase-4 (1:200, Santa Cruz Cat#1229), anti-mouse caspase-11 (1:200, Novus Rat mAb 17D9 Cat#NB120-10454, or 1: 1000 Abcam Rabbit mAb Cat# ab180673 1:500), anti-STAT2 (1:500, Cell Signaling, Cat #72604), anti-pSTAT2 (1:250, Millipore Cat# 07-224), anti-human cGAS (1:1000, Cell Signaling Cat# 15102), anti-VDAC-1 (1:1000, Cell Signaling Cat# #4661), anti-mouse IRF3 (1:500, Novus Biologicals, Cat#NBP1-78769), anti-phospho-IRF3 (1:500, Cell Signaling Cat# 4947S, Cat# 29047), anti-HA-tag (1:1000; Cell Signaling Cat# 2367), anti-α-tubulin mouse mAb (1:50000, Sigma-Aldrich), anti-β-actin mouse mAb (1:50000, Sigma-Aldrich), anti-vinculin (1:2000, Sigma-Aldrich), anti-cleaved caspase-3 (1:500, Cell Signaling Cat#9661), anti-PARP (1:1000, Cell Signaling Cat#9542), anti-human GSDMD gasdermin D (1:500, Abcam Cat#ab57785) and anti-mouse gasdermin D mAb (1 μg/mL; a generous gift from V.M Dixit (Genentech). Immunoblotting for activated Caspase 1 in the supernatant was performed as described earlier[19]. Briefly, supernatants were collected and were briefly spun down to remove floating cells. Proteins from the cell-free supernatant were precipitated by adding sodium deoxycholate (0.15% final) followed by adding TCA (7.2% final) and incubating on ice for 30 min to overnight. Samples were spun down at 13000g for 30 mins and pellets were washed 2 times with ice-cold acetone. Precipitated proteins solubilized in 4X LDS Buffer with 2-mercaptoethanol were used for immunoblotting.

Cell Culture

Primary mouse and human RPE cells were isolated as previously described[79]. All cells were maintained at 37 °C and 5% CO_2 environment. Mouse RPE cells were cultured in Dulbecco Modified Eagle Medium (DMEM) supplemented with 20% FBS and penicillin/streptomycin antibiotics at standard concentrations; primary human RPE cells were maintained in DMEM supplemented with 10% FBS and antibiotics. The human RPE cell line ARPE19 and ARPE19 cells lacking mitochondrial DNA (Rho^0 ARPE19) were cultured as described earlier[80]. Rho^0 ARPE19 cells were maintained at 37 °C in 24 mM Na_2HCO_3, 10% FBS, 50 μg/ml uridine, 1 mM sodium pyruvate in DMEM-F12 (Gibco, Cat#11320-033) containing pen/strep, Fungizone, and gentamicin. ARPE19 cells were maintained in DMEM-F12 containing pen/strep, Fungizone, and gentamicin. Bone marrow derived macrophages (BMDM) were cultured in DMEM with 10% fetal bovine serum and 20% L929 supernatants. *Mb21d1*$^{-/-}$ and HA-cGAS reconstituted *Mb21d1*$^{-/-}$ mouse embryonic fibroblasts were cultured in DMEM with 10% FBS and antibiotics[30].

Synthesis of *in vitro* transcribed *Alu* RNA

T7 promoter containing *Alu* expression plasmid was linearized and used for generating *in vitro* transcribed *Alu* RNA using AmpliScribe T7-Flash Transcription Kit (Epicenter) following the manufacturer’s instructions. The resulting *Alu* RNA was DNase treated and purified using MEGAclear (Ambion), and its integrity was monitored by gel electrophoresis[4,5].

Transfection

Alu expression plasmid (pAlu), empty vector control (pNull) *in vitro* transcribed *Alu* RNA were transfected into human and mouse RPE cells using Lipofectamine 2000 (Invitrogen) following the manufacturer’s instructions. mtDNA prepared as described below was transfected into mouse RPE cells using Lipofectamine 2000 (Invitrogen) following the manufacturer’s instructions.

LPS transfection into BMDM

Approximately 2×10^6 BMDM cells were cultured overnight at 37 °C in a 60-mm dish. After 4–6 h of priming with 1 μg/ml Pam3CSK4 (Invivogen, Cat# tlrl-pms), the cells were transfected with LPS (5 μg/ml final concentration, Invivogen, Cat# tlrl-3pelps, ultrapure) with FugeneHD (Promega, Cat# E2311) using a standard transfection protocol. 16 h post-transfection, cell lysates were collected and analyzed.

Extraction of mitochondria-free cytosolic fractions

Human and mouse RPE cells were either mock treated or stimulated with *Alu* RNA. 24 h post *Alu* RNA transfection or 48 h post scrambled or DICER1 AS oligonucleotide transfection, the cells were harvested by trypsinization. 2×10^6 cells were used for collecting mitochondria-free cytosolic fractions using the Mitochondrial Isolation kit (Thermo Scientific Cat#89874). Briefly, cells were resuspended in 800 μl of Reagent A and were placed on ice for 2 min; the suspension was then dounce homogenized (10 strokes) to lyse the cells and to release nuclei, and then the suspension was incubated for 5 min on ice after addition of 10 µL Reagent B, with vortexing every minute. To this suspension 800 µl Mitochondria Isolation Reagent C was added and the resulting suspension was centrifuged at 700 g for 10 min at 4 °C to pellet the nuclei. The supernatant containing the cytoplasmic fraction was centrifuged at 700 g for 10 min at 4 °C for a total of five times to completely remove nuclei or any unlysed cells. The resulting nuclei-free cytoplasmic fraction was centrifuged at 13,000g for 15 min at 4 °C to pellet the mitochondria. The resulting supernatant was further centrifuged at 13,000g for 15 min at 4 °C for an additional six times to remove all the mitochondria. The supernatant was then tested for an absence of mitochondria by immunoblotting for the mitochondrial marker protein VDAC and the cytosolic marker protein tubulin.

Reconstitution experiment

Mb21d1$^{-/-}$ mouse RPE cells were transfected with 2 µg cGAS expression plasmid[26] or empty vector in a 60 mm dish at 70–80% confluency. 24 h post transfection, cells were plated on 6-well dishes. 24 h post plating, cells were transfected with *Alu* RNA (50 pmol) or were mock transfected using Lipofectamine 2000. 18 h post *Alu* RNA transfection, cells were collected for RNA extraction to examine induction of IFN-β mRNA. For Caspase-11 reconstitution. *Casp11*$^{-/-}$ mouse RPE cells were transduced with control or caspase-11 expressing lentiviral particles. The transduced cells were allowed to rest for three days and the cells were then plated in a 60 mm dish at 70–80% confluency. Control or Caspase-11 reconstituted *Casp11*$^{-/-}$ cells were mock treated or stimulated with Alu RNA as described above and activation of caspase-1 was assessed by western blotting. For the caspase-1 activity assay, *Casp11*$^{-/-}$ mouse RPE cells transfected with caspase-11 expression plasmid (pCasp11) or empty vector (pNull) were exposed to *Alu* RNA as described above and caspase-1 activity was assessed using the CaspaLux®1-E_1D_2 kit (OncoImmunin Cat # CPL1R1E-5). Quantification of the CaspaLux signal was performed by a blinded operator measuring the integrated density of fluorescent micrographs using Image J software (NIH) and normalizing to the number of cells.

Lentiviral transduction

Lentivirus particles were produced either by the University of Kentucky Viral Production Core facilities or in house. Lentivirus vector plasmids expressing scrambled sequences or shRNA sequences targeting human caspase-4 (Sigma Aldrich, #TRCN0000003511) and cGAS (Sigma Aldrich# TRCN0000150010) were purchased (MISSION®shRNA, Sigma-Aldrich) to produce lentiviral particles. Human RPE cells at passage 3 were incubated with lentiviral particles at a multiplicity of infection (MOI) of 5 overnight in regular growth media containing polybrene (4 µg/ml). On day 2, cells were washed, incubated in regular growth media and allowed to rest for 24 h. Lentivirus transduced cells were then cultured under puromycin (5 µg/ml) selection pressure for 5 days. Knock-down of the target proteins was determined by immunoblotting.

Enzyme-linked immunosorbent assay (ELISA)

Secreted human and mouse interferon-β and IL-18 in the media were detected using ELISA kits (mouse IFN-β, R&D Systems Cat# 42400-1; mouse IL-18, R&D Systems Cat# 7625; human IFN-β, R&D Systems Cat# 41410; human IL-18, R&D systems Cat# DY318-05) according to the manufacturer′s instructions. Primary mouse cells were cultured as above. WT, *Gsdmd*$^{-/-}$, *Casp11*$^{-/-}$, or *Mb21d1*$^{-/-}$ mouse RPE cells were seeded at a density of 250,000 cells/well in a 12-well plate. When confluency reached 60–70%, cells were transfected with 20 pmol of *in vitro* transcribed *Alu* RNA or mock using Lipofectamine 2000 reagent (Life Technologies, Carlsbad, CA) following the manufacturer's protocol. Media was collected to detect secreted cytokine content at 8 to 24 h post-transfection. For examination of the induction of IL-18 secretion by monosodium urate (MSU) crystals (Invivogen Cat# tlrl-msu), mouse RPE cells were primed with LPS (500 ng/ml) for 6 h and exposed to MSU (250 μg/ml) for 16 h, and media was collected to detect secreted cytokine.

cGAS-mtDNA interaction Immunoprecipitation assay

Immortalized *cGAS*$^{-/-}$ mouse embryonic fibroblasts (MEF) reconstituted with HA-tagged mouse cGAS (HA-cGAS) were described earlier[30]. The interaction between mtDNA and cGAS was monitored using Express Chromatin Immunoprecipitation Kit (Active Motif, ChIP-IT® Express, cat# 53008). Briefly mock, *Alu* RNA, poly I:C or plasmid DNA (pUC19) transfected HA-cGAS reconstituted *cGAS*$^{-/-}$ MEFs were fixed with 1% formaldehyde per the manufacturer's instructions. The cells were then lysed by sonication in the shearing buffer and centrifuged for 10 min at 18,000g in a 4 °C microfuge. The supernatant containing the cell lysate was collected and cGAS was immunoprecipitated from each sample using anti-HA tag antibody (Abcam, cat# ab9110). DNA in the IP was eluted, reverse crosslinked and purified using the Chromatin IP DNA Purification Kit (Active Motif, cat# 58002). Purified DNA was analyzed by qPCR using mouse mtDNA specific primer pairs. The fold enrichment of mtDNA in HA-cGAS immunoprcipitates in cells exposed to *Alu* RNA compared to mock transfected cells was calculated.

Quantification of PAPC and oxPAPC by LC-MS

Human RPE cells, mock-stimulated or stimulated with *Alu* RNA, were washed with cold PBS and trypsinized at 24 h post-stimulation. The cells were washed with cold PBS and 2×10^6 cells were used for lipid extraction by a modified Bligh-Dyer extraction method[81]. Briefly, the cell pellet was manually homogenized and then mixed in a glass tube with 700 μL HPLC-grade chloroform and 300 μL HPLC-grade Methanol (Sigma) supplemented with 0.01% butylated hydroxytoluene (BHT from Sigma) and 189 nmol of the internal standard, di-nonanoyl-phosphatidylcholine (DNPC from Avanti). 1 mL of HPLC-grade water was added and the mixture was vigorously vortexed for 60 sec. Next, the mixture was centrifuged (1,000 rpm for 10 min) to separate the fractions and the organic layer (bottom) was removed and placed into a fresh glass tube. 1 mL of chloroform was added to the aqueous fraction and the extraction was performed once more. The organic layer of the second extraction was combined with the first, and then dried down under nitrogen. Upon complete evaporation of the organic solvent, the lipids were suspended in 300 μL of Solvent A (69% water; 31% methanol; 10 mM ammonium acetate) and stored at −80 °C. The determination and quantification of oxidized phosphatidylcholine and phosphatidylethanolamine species was performed by liquid chromatography-linked ESI mass spectrometry, using an ABI Sciex 4000 QTrap. Separation of the phospholipids was achieved by loading samples onto a C8 column (Kinetex 5 μm, 150×4.6mm from Phenomenex). Elution of the phospholipids was achieved using a binary gradient with

Solvent A (69% water; 31% methanol; 10 mM ammonium acetate) and Solvent B (50% methanol; 50% isopropanol; 10 mM ammonium acetate) as the mobile phases. Detection for phosphatidylcholine (PC) was conducted using multiple reaction monitoring (MRM) in positive mode by identification of two transition states for each analyte. Quantification of each analyte was performed based on the peak area of the 184 m/z fragment ion for PC.

Determination of mitochondrial permeability transition pore opening

Mitochondrial permeability transition pore (mPTP) opening in WT and *Ppif*$^{-/-}$ mouse RPE cells was monitored by the calcein-Co^{2+} technique[82] using the Mitochondrial Permeability Transition Pore Assay Kit (Biovision Inc Cat# K239-100). Mitochondrial membrane potential was evaluated with the JC-1 fluorochrome-based MITO-ID® Membrane Potential Cytotoxicity Kit (Enzo Cat# ENZ-51019-KP002)[83]. mPTP opening was inhibited by performing the above assays using cyclosporine A (10 μM)-containing media. The assay was performed in a 96-well microtiter plate according to the manufacturer’s instructions.

Live Cell Imaging

2×10^4 human RPE cells were plated on each well of an 8-well chambered slide (Thermo Scientific Cat#155411). 18–24 h after plating, cells were transfected with 11.5 pmol *in vitro* transcribed *Alu* RNA (using Lipofectamine 2000) in culture medium supplemented with 2.5 mM $CaCl_2$ and annexin-V 488 (1:200, Invitrogen V13241) and propidium iodide (1:1500, Invitrogen Cat#P3566). Immediately following transfection, annexin V, propidium iodide, and DIC signals were acquired using a Nikon A1R confocal microscope equipped with an automated stage. Images were captured at 3 min intervals for a total duration of 50 h. Cells were maintained at 37 °C and 5% CO_2 for the duration of the imaging study via a stage top incubator.

RPE flat mount annexin V/PI-staining

Mouse RPE/choroid flat mounts prepared in DMEM with 10% FBS were washed with binding buffer once and then incubated with Alexa Fluor™ 647 conjugated Annexin V (Invitrogen) for 15 min. The annexin V stained mouse RPE/choroid flat mounts were fixed with 2% paraformaldehyde for 30 min, stained with propidium iodide (PI) containing RNase (Invitrogen) for 30 min and mounted using ProLong™ Gold Antifade Mountant solution (Thermo Fisher Scientific).

Microglia depletion

Microglia were depleted by administering tamoxifen to *CX3CR1*^{CreER}; DTA^{flox} mice which express Cre-ER under control of microglia specific CX3CR1 promoter and also contain flox-STOP-flox diphtheria toxin subunit α (*DTA*) gene cassette in the *ROSA26* locus (DTA^{flox}). *Cx3cr1*^{CreER}; DTA^{flox} mice were generated by breeding heterozygous *Cx3cr1*^{CreER} mice with DTA^{flox} mice (both mouse strains were generous gifts from Wai T. Wong and Lian Zhao, NIH). To deplete microglia, tamoxifen was administered to *Cx3cr1*^{CreER}; DTA^{flox} mice as described earlier[35]. Briefly, adult 2- to 3-month-old TG mice were administered with tamoxifen (TAM) dissolved in corn oil (Sigma-Aldrich; 500 mg/kg dose of a 20 mg/ml solution) via oral gavage (Schedule: days −2, 0, 5, 10, and 15). On day

11, *Alu* RNA was delivered via subretinal injection. *Alu* RNA-induced RPE degeneration was assessed as described above. Microglial depletion was confirmed by staining retinal flat mounts for F4/80. Briefly retinal flat mounts were prepared and fixed in 2% paraformaldehyde for 1 h, and stained with RPE conjugated F4/80 (Bio-Rad, Cat# MCA497PET) and fluorescein labeled Griffonia Simplicifolia Lectin isolectin B4 (IB4, Vector Laboratories, Cat# FL-1201). All images were obtained using Zeiss Axio Observer Z1 microscope.

Macrophage depletion

Depletion of macrophages was achieved via administering clodronate liposomes, which eliminates macrophages, in wild-type mice[34]. Briefly, animals received 200 μl clodronate liposomes (Liposoma Cat# LIP-01) through the tail vein on days −2 and day 0. *Alu* RNA or vehicle control were subretinally injected immediately after the day 0 tail vein injection.

Statistical Analyses

Real-time qPCR and ELISA data are expressed as means ± standard error of the mean (SEM) were analyzed using Student t test. The binary readouts of RPE degeneration (i.e., presence or absence of RPE degeneration on fundus and ZO-1-stained flat mount images) were analyzed using Fisher's exact test. Cell morphometry data were assessed using Student t test. P values < 0.05 were deemed statistically significant. Sample sizes were selected based on power analysis α=5%; 1–β = 80%, such that we could detect a minimum of 50% change assuming a sample SD based on Bayesian inference. Outliers were assessed by Grubbs' test. Based on this analysis no outliers were detected and no data were excluded. Fewer than 5% of subretinal injection recipient tissues were excluded based on predetermined exclusion criteria (hemorrhage and animal death due to anesthesia complications, etc.) relating to the technical challenges of this delicate procedure.

Supplementary Material

Refer to Web version on PubMed Central for supplementary material.

Acknowledgments

We thank Z. Chen, V. Tarallo, and P. Pinton for valuable discussions; H. Virgin for *Mb21d1*$^{-/-}$ MEFs; G. Shadel (Yale University) for immortalized HA-cGAS reconstituted *Mb21d1*$^{-/-}$ MEFs; and W.T. Wong and L. Zhao (NIH) for *Cx3cr1*^{CreER} ROSA-DTA mice. We thank G. Pattison, E. Ghias, K. Langberg, D. Robertson, E. Doswell, X. Zhou, K. Atwood, R. Makin, O. Kirillina, A. Bobrov, E. Dinning, L. Pandya, C. Payne, G. Botzet, N. Bell, R. King, L. Xu, L. Toll, and A. Uittenbogaard for their technical assistance, and University of Kentucky Viral Core (COBRE) for providing lentivirus vectors. J.A. was supported by NIH grants (DP1GM114862, R01EY018350, R01EY018836, R01EY020672, R01EY022238, and R01EY024068), Doris Duke Distinguished Clinical Scientist Award, Burroughs Wellcome Fund Clinical Scientist Award in Translational Research, Ellison Medical Foundation Senior Scholar in Aging Award, John Templeton Foundation, Dr. E. Vernon Smith and Eloise C. Smith Macular Degeneration Endowed Chair, and DuPont Guerry, III, Professorship; N.K. by NIH (K99EY024336, R00EY024336) and Beckman Initiative for Macular Research (BIMR); B.J.F by NIH T32HL091812 and UL1RR033173; R.Y. by Association for Research in Vision and Ophthalmology (ARVO)/Alcon Early Career Clinician-Scientist Research Award; T.Y. by Fight for Sight postdoctoral award; A.B.C. by the Programme for Advanced Medical Education (sponsored by Fundação Calouste Gulbenkian, Fundação Champalimaud, Ministério da Saúde and Fundação para a Ciência e Tecnologia, Portugal); D.R.H. by NIH R01EY001545 and an unrestricted departmental grant from Research to Prevent Blindness; J.C.C. by NIH R21AI099346; S.F.by Research Grant of Japan Eye Bank Association; S.M.J. by NIH R37AG006168; B.D.G. by American Heart Association and by the National Center for Research Resources and the National Center for Advancing Translational Sciences, National

Institutes of Health, through Grant UL1TR000117; V.S. by NIH (T32GM007055; F31DK108553) and N.L. by NIH (R01DK096076, P01 HL120840). The content is solely the responsibility of the authors and does not necessarily represent the official views of the NIH.

References

1. Wong WL, et al. Global prevalence of age-related macular degeneration and disease burden projection for 2020 and 2040: a systematic review and meta-analysis. Lancet Glob Health. 2014; 2:e106–116. [PubMed: 25104651]
2. Ambati J, Ambati BK, Yoo SH, Ianchulev S, Adamis AP. Age-related macular degeneration: etiology, pathogenesis, and therapeutic strategies. Surv Ophthalmol. 2003; 48:257–293. [PubMed: 12745003]
3. Ambati J, Atkinson JP, Gelfand BD. Immunology of age-related macular degeneration. Nat Rev Immunol. 2013; 13:438–451. [PubMed: 23702979]
4. Kaneko H, et al. DICER1 deficit induces Alu RNA toxicity in age-related macular degeneration. Nature. 2011; 471:325–330. [PubMed: 21297615]
5. Tarallo V, et al. DICER1 loss and Alu RNA induce age-related macular degeneration via the NLRP3 inflammasome and MyD88. Cell. 2012; 149:847–859. [PubMed: 22541070]
6. Anderson OA, Finkelstein A, Shima DT. A2E induces IL-1ss production in retinal pigment epithelial cells via the NLRP3 inflammasome. PloS one. 2013; 8:e67263. [PubMed: 23840644]
7. Tseng WA, et al. NLRP3 Inflammasome Activation in Retinal Pigment Epithelial Cells by Lysosomal Destabilization: Implications for Age-Related Macular Degeneration. Investigative ophthalmology & visual science. 2013; 54:110–120. [PubMed: 23221073]
8. Gelfand BD, et al. Iron Toxicity in the Retina Requires Alu RNA and the NLRP3 Inflammasome. Cell Rep. 2015; 11:1686–1693. [PubMed: 26074074]
9. Kayagaki N, et al. Noncanonical inflammasome activation by intracellular LPS independent of TLR4. Science. 2013; 341:1246–1249. [PubMed: 23887873]
10. Rathinam VA, et al. TRIF licenses caspase-11-dependent NLRP3 inflammasome activation by gram-negative bacteria. Cell. 2012; 150:606–619. [PubMed: 22819539]
11. Zanoni I, et al. An endogenous caspase-11 ligand elicits interleukin-1 release from living dendritic cells. Science. 2016; 352:1232–1236. [PubMed: 27103670]
12. Kayagaki N, et al. Non-canonical inflammasome activation targets caspase-11. Nature. 2011; 479:117–121. [PubMed: 22002608]
13. Kleinman ME, et al. Sequence- and target-independent angiogenesis suppression by siRNA via TLR3. Nature. 2008; 452:591–597. [PubMed: 18368052]
14. Kleinman ME, et al. Short-interfering RNAs induce retinal degeneration via TLR3 and IRF3. Molecular therapy: the journal of the American Society of Gene Therapy. 2012; 20:101–108. [PubMed: 21988875]
15. Kajiwara Y, et al. A critical role for human caspase-4 in endotoxin sensitivity. J Immunol. 2014; 193:335–343. [PubMed: 24879791]
16. Fowler BJ, et al. Nucleoside reverse transcriptase inhibitors possess intrinsic anti-inflammatory activity. Science. 2014; 346:1000–1003. [PubMed: 25414314]
17. Kerur N, et al. TLR-independent and P2X7-dependent signaling mediate Alu RNA-induced NLRP3 inflammasome activation in geographic atrophy. Investigative ophthalmology & visual science. 2013; 54:7395–7401. [PubMed: 24114535]
18. Shi J, et al. Cleavage of GSDMD by inflammatory caspases determines pyroptotic cell death. Nature. 2015; 526:660–665. [PubMed: 26375003]
19. Kayagaki N, et al. Caspase-11 cleaves gasdermin D for non-canonical inflammasome signalling. Nature. 2015; 526:666–671. [PubMed: 26375259]
20. Liu X, et al. Inflammasome-activated gasdermin D causes pyroptosis by forming membrane pores. Nature. 2016; 535:153–158. [PubMed: 27383986]
21. Aglietti RA, et al. GsdmD p30 elicited by caspase-11 during pyroptosis forms pores in membranes. Proc Natl Acad Sci U S A. 2016; 113:7858–7863. [PubMed: 27339137]

22. Kim Y, et al. DICER1/Alu RNA dysmetabolism induces Caspase-8-mediated cell death in age-related macular degeneration. Proc Natl Acad Sci U S A. 2014; 111:16082–16087. [PubMed: 25349431]
23. Dunaief JL, Dentchev T, Ying GS, Milam AH. The role of apoptosis in age-related macular degeneration. Arch Ophthalmol. 2002; 120:1435–1442. [PubMed: 12427055]
24. van Genderen H, et al. In vitro measurement of cell death with the annexin A5 affinity assay. Nat Protoc. 2006; 1:363–367. [PubMed: 17406257]
25. Fink SL, Bergsbaken T, Cookson BT. Anthrax lethal toxin and Salmonella elicit the common cell death pathway of caspase-1-dependent pyroptosis via distinct mechanisms. Proc Natl Acad Sci U S A. 2008; 105:4312–4317. [PubMed: 18337499]
26. Sun L, Wu J, Du F, Chen X, Chen ZJ. Cyclic GMP-AMP synthase is a cytosolic DNA sensor that activates the type I interferon pathway. Science. 2013; 339:786–791. [PubMed: 23258413]
27. Schoggins JW, et al. Pan-viral specificity of IFN-induced genes reveals new roles for cGAS in innate immunity. Nature. 2014; 505:691–695. [PubMed: 24284630]
28. Feher J, et al. Mitochondrial alterations of retinal pigment epithelium in age-related macular degeneration. Neurobiol Aging. 2006; 27:983–993. [PubMed: 15979212]
29. Terluk MR, et al. Investigating mitochondria as a target for treating age-related macular degeneration. The Journal of neuroscience: the official journal of the Society for Neuroscience. 2015; 35:7304–7311. [PubMed: 25948278]
30. West AP, et al. Mitochondrial DNA stress primes the antiviral innate immune response. Nature. 2015; 520:553–557. [PubMed: 25642965]
31. Galluzzi L, Blomgren K, Kroemer G. Mitochondrial membrane permeabilization in neuronal injury. Nat Rev Neurosci. 2009; 10:481–494. [PubMed: 19543220]
32. Baines CP, et al. Loss of cyclophilin D reveals a critical role for mitochondrial permeability transition in cell death. Nature. 2005; 434:658–662. [PubMed: 15800627]
33. McLeod DS, et al. Distribution and Quantification of Choroidal Macrophages in Human Eyes With Age-Related Macular Degeneration. Investigative ophthalmology & visual science. 2016; 57:5843–5855. [PubMed: 27802514]
34. Sakurai E, Anand A, Ambati BK, van Rooijen N, Ambati J. Macrophage depletion inhibits experimental choroidal neovascularization. Investigative ophthalmology & visual science. 2003; 44:3578–3585. [PubMed: 12882810]
35. Wang X, et al. Requirement for Microglia for the Maintenance of Synaptic Function and Integrity in the Mature Retina. The Journal of neuroscience: the official journal of the Society for Neuroscience. 2016; 36:2827–2842. [PubMed: 26937019]
36. Karijolich J, Abernathy E, Glaunsinger BA. Infection-Induced Retrotransposon-Derived Noncoding RNAs Enhance Herpesviral Gene Expression via the NF-kappaB Pathway. PLoS pathogens. 2015; 11:e1005260. [PubMed: 26584434]
37. Nunnari J, Suomalainen A. Mitochondria: in sickness and in health. Cell. 2012; 148:1145–1159. [PubMed: 22424226]
38. West AP, Shadel GS, Ghosh S. Mitochondria in innate immune responses. Nat Rev Immunol. 2011; 11:389–402. [PubMed: 21597473]
39. Fang C, Wei X, Wei Y. Mitochondrial DNA in the regulation of innate immune responses. Protein Cell. 2016; 7:11–16. [PubMed: 26498951]
40. Shimada K, et al. Oxidized mitochondrial DNA activates the NLRP3 inflammasome during apoptosis. Immunity. 2012; 36:401–414. [PubMed: 22342844]
41. Nakahira K, et al. Autophagy proteins regulate innate immune responses by inhibiting the release of mitochondrial DNA mediated by the NALP3 inflammasome. Nat Immunol. 2011; 12:222–230. [PubMed: 21151103]
42. Zhang Q, Itagaki K, Hauser CJ. Mitochondrial DNA is released by shock and activates neutrophils via p38 map kinase. Shock. 2010; 34:55–59. [PubMed: 19997055]
43. Yan Y, et al. Dicer expression exhibits a tissue-specific diurnal pattern that is lost during aging and in diabetes. PloS one. 2013; 8:e80029. [PubMed: 24244599]

44. Hung T, et al. The Ro60 autoantigen binds endogenous retroelements and regulates inflammatory gene expression. Science. 2015; 350:455–459. [PubMed: 26382853]

45. Hitomi J, et al. Involvement of caspase-4 in endoplasmic reticulum stress-induced apoptosis and Abeta-induced cell death. The Journal of cell biology. 2004; 165:347–356. [PubMed: 15123740]

46. Katayama T, et al. Presenilin-1 mutations downregulate the signalling pathway of the unfolded-protein response. Nat Cell Biol. 1999; 1:479–485. [PubMed: 10587643]

47. Ozcan U, et al. Endoplasmic reticulum stress links obesity, insulin action, and type 2 diabetes. Science. 2004; 306:457–461. [PubMed: 15486293]

48. Yang D, He Y, Munoz-Planillo R, Liu Q, Nunez G. Caspase-11 Requires the Pannexin-1 Channel and the Purinergic P2X7 Pore to Mediate Pyroptosis and Endotoxic Shock. Immunity. 2015; 43:923–932. [PubMed: 26572062]

49. Shaw PX, et al. Complement factor H genotypes impact risk of age-related macular degeneration by interaction with oxidized phospholipids. Proc Natl Acad Sci U S A. 2012; 109:13757–13762. [PubMed: 22875704]

50. Suzuki M, et al. Oxidized phospholipids in the macula increase with age and in eyes with age-related macular degeneration. Mol Vis. 2007; 13:772–778. [PubMed: 17563727]

51. Brandstetter C, Mohr LK, Latz E, Holz FG, Krohne TU. Light induces NLRP3 inflammasome activation in retinal pigment epithelial cells via lipofuscin-mediated photooxidative damage. J Mol Med (Berl). 2015; 93:905–916. [PubMed: 25783493]

52. Kauppinen A, et al. Oxidative stress activates NLRP3 inflammasomes in ARPE-19 cells–implications for age-related macular degeneration (AMD). Immunology letters. 2012; 147:29–33. [PubMed: 22698681]

53. Marneros AG. NLRP3 inflammasome blockade inhibits VEGF-A-induced age-related macular degeneration. Cell Rep. 2013; 4:945–958. [PubMed: 24012762]

54. Doyle SL, et al. NLRP3 has a protective role in age-related macular degeneration through the induction of IL-18 by drusen components. Nature medicine. 2012; 18:791–798.

55. Wallach D, Kang TB, Dillon CP, Green DR. Programmed necrosis in inflammation: Toward identification of the effector molecules. Science. 2016; 352:aaf2154. [PubMed: 27034377]

56. Man SM, Kanneganti TD. Converging roles of caspases in inflammasome activation, cell death and innate immunity. Nat Rev Immunol. 2016; 16:7–21. [PubMed: 26655628]

57. Hirano Y, et al. IL-18 is not therapeutic for neovascular age-related macular degeneration. Nature medicine. 2014; 20:1372–1375.

58. Wiesen JL, Tomasi TB. Dicer is regulated by cellular stresses and interferons. Mol Immunol. 2009; 46:1222–1228. [PubMed: 19118902]

59. van den Beucken T, et al. Hypoxia promotes stem cell phenotypes and poor prognosis through epigenetic regulation of DICER. Nat Commun. 2014; 5:5203. [PubMed: 25351418]

60. Ambati J, Fowler BJ. Mechanisms of age-related macular degeneration. Neuron. 2012; 75:26–39. [PubMed: 22794258]

61. Mariathasan S, et al. Differential activation of the inflammasome by caspase-1 adaptors ASC and Ipaf. Nature. 2004; 430:213–218. [PubMed: 15190255]

62. Kanneganti TD, et al. Bacterial RNA and small antiviral compounds activate caspase-1 through cryopyrin/Nalp3. Nature. 2006; 440:233–236. [PubMed: 16407888]

63. Muller U, et al. Functional role of type I and type II interferons in antiviral defense. Science. 1994; 264:1918–1921. [PubMed: 8009221]

64. Sato M, et al. Distinct and essential roles of transcription factors IRF-3 and IRF-7 in response to viruses for IFN-alpha/beta gene induction. Immunity. 2000; 13:539–548. [PubMed: 11070172]

65. Suschak JJ, Wang S, Fitzgerald KA, Lu S. A cGAS-Independent STING/IRF7 Pathway Mediates the Immunogenicity of DNA Vaccines. J Immunol. 2016; 196:310–316. [PubMed: 26590319]

66. Jin L, et al. MPYS is required for IFN response factor 3 activation and type I IFN production in the response of cultured phagocytes to bacterial second messengers cyclic-di-AMP and cyclic-di-GMP. J Immunol. 2011; 187:2595–2601. [PubMed: 21813776]

67. Bennett EA, et al. Active Alu retrotransposons in the human genome. Genome research. 2008; 18:1875–1883. [PubMed: 18836035]

68. Shaikh TH, Roy AM, Kim J, Batzer MA, Deininger PL. cDNAs derived from primary and small cytoplasmic Alu (scAlu) transcripts. Journal of molecular biology. 1997; 271:222–234. [PubMed: 9268654]
69. Nagai H, et al. Gene transfer of secreted-type modified interleukin-18 gene to B16F10 melanoma cells suppresses in vivo tumor growth through inhibition of tumor vessel formation. J Invest Dermatol. 2002; 119:541–548. [PubMed: 12230493]
70. Huang J, et al. Comparison of Noncontact Specular and Confocal Microscopy for Evaluation of Corneal Endothelium. Eye Contact Lens. 2017
71. Laing RA, Sanstrom MM, Berrospi AR, Leibowitz HM. Changes in the corneal endothelium as a function of age. Exp Eye Res. 1976; 22:587–594. [PubMed: 776638]
72. Doughty MJ, Muller A, Zaman ML. Assessment of the reliability of human corneal endothelial cell-density estimates using a noncontact specular microscope. Cornea. 2000; 19:148–158. [PubMed: 10746445]
73. Inaba M, Matsuda M, Shiozaki Y, Kosaki H. Regional specular microscopy of endothelial cell loss after intracapsular cataract extraction: a preliminary report. Acta Ophthalmol (Copenh). 1985; 63:232–235. [PubMed: 4003052]
74. Laing RA, Sandstrom MM, Leibowitz HM. In vivo photomicrography of the corneal endothelium. Arch Ophthalmol. 1975; 93:143–145. [PubMed: 1115675]
75. Ach T, et al. Lipofuscin redistribution and loss accompanied by cytoskeletal stress in retinal pigment epithelium of eyes with age-related macular degeneration. Investigative ophthalmology & visual science. 2015; 56:3242–3252. [PubMed: 25758814]
76. Dridi S, et al. ERK1/2 activation is a therapeutic target in age-related macular degeneration. Proc Natl Acad Sci U S A. 2012; 109:13781–13786. [PubMed: 22869729]
77. Grossniklaus HE, Nickerson JM, Edelhauser HF, Bergman LA, Berglin L. Anatomic alterations in aging and age-related diseases of the eye. Investigative ophthalmology & visual science. 2013; 54:ORSF23–27. [PubMed: 24335063]
78. Bannwarth S, Procaccio V, Paquis-Flucklinger V. Rapid identification of unknown heteroplasmic mutations across the entire human mitochondrial genome with mismatch-specific Surveyor Nuclease. Nat Protoc. 2006; 1:2037–2047. [PubMed: 17487193]
79. Yang P, Tyrrell J, Han I, Jaffe GJ. Expression and modulation of RPE cell membrane complement regulatory proteins. Investigative ophthalmology & visual science. 2009; 50:3473–3481. [PubMed: 19168900]
80. Miceli MV, Jazwinski SM. Nuclear gene expression changes due to mitochondrial dysfunction in ARPE-19 cells: implications for age-related macular degeneration. Investigative ophthalmology & visual science. 2005; 46:1765–1773. [PubMed: 15851580]
81. Kagan VE, et al. Oxidized arachidonic and adrenic PEs navigate cells to ferroptosis. Nat Chem Biol. 2017; 13:81–90. [PubMed: 27842066]
82. Wang X, et al. Polydatin, a natural polyphenol, protects arterial smooth muscle cells against mitochondrial dysfunction and lysosomal destabilization following hemorrhagic shock. Am J Physiol Regul Integr Comp Physiol. 2012; 302:R805–814. [PubMed: 22277937]
83. Bonora M, et al. Comprehensive analysis of mitochondrial permeability transition pore activity in living cells using fluorescence-imaging-based techniques. Nat Protoc. 2016; 11:1067–1080. [PubMed: 27172167]

Editorial summary

Degeneration of the retinal pigment epithelium is a hallmark of geographic atrophy, a type of age-related macular degeneration. Kerur *et al.* show that this degeneration results from a multi-step pathway in which mitochondrial dysfunction in RPE cells, triggered by accumulation of *Alu* RNA, leads to activation of the non-canonical inflammasome via a cGAS-STING-IRF3 signaling axis.

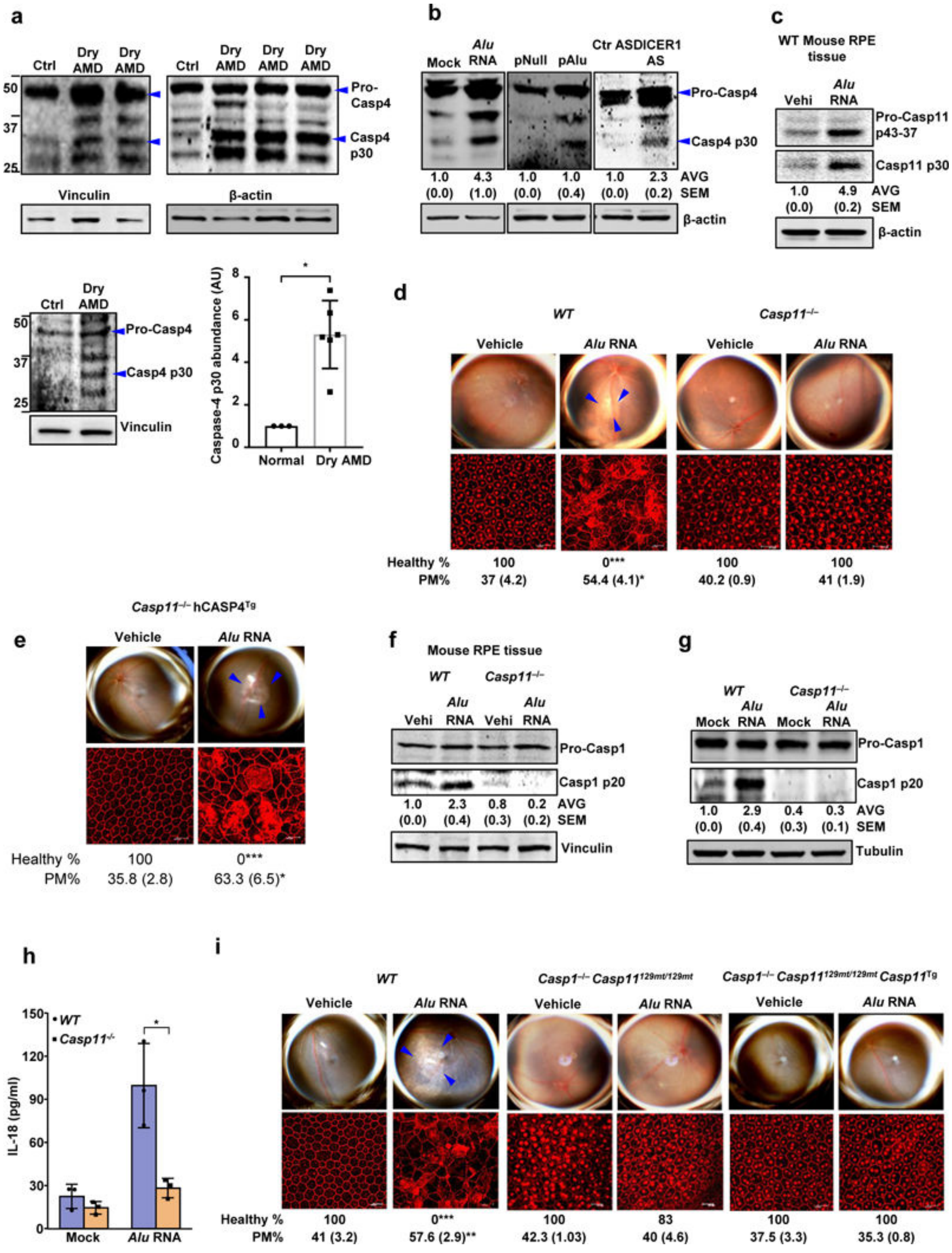

Figure 1. Caspase-4/11 in geographic atrophy and RPE degeneration

(**a**) Left and top quadrants, immunoblots for pro-caspase-4 (pro-Casp4) and the p30 cleavage product of caspase-4 (Casp4 p30) in the RPE of human eyes with geographic atrophy (dry AMD) as compared to unaffected controls (Ctr). Specific bands of interest are indicated by arrowheads. Lower right quadrant, densitometry of the bands corresponding to caspase-4 p30 normalized to loading control. The molecular weight markers are indicated on the left side of the blot (Data are presented as mean ± SD; n = 3 control eyes; n = 6 dry AMD eyes; *P = 0.002, two-tailed t test). (**b**) Immunoblots for pro-Casp4 and Casp4 p30 in human RPE cells mock transfected (just transfection mixture) or transfected with *Alu* RNA; *Alu* expression plasmid (pAlu) or empty vector (pNull); or DICER1 or control (Ctr) anti-sense oligonucleotides (AS). Specific bands of interest are indicated by arrowheads. (**c**) Immunoblot for pro-caspase-11 (Pro-Casp11) and the p30 cleavage product of caspase-11 (Casp11 p30) in RPE tissue of WT mice injected subretinally with *Alu* RNA or vehicle (Vehi). *n* = 3 mice per group. (d,e) Top, fundus photographs of the retinas of WT (n = 8 eyes) and $Casp11^{-/-}$ (n = 10 eyes) mice, (**d**) and $Casp11^{-/-}$ (n = 8 eyes) mice expressing a human caspase-4 transgene ($Casp11^{-/-}$ $hCasp4^{Tg}$) (**e**) injected with vehicle or *Alu* RNA. The degenerated retinal area is outlined by blue arrowheads. Bottom, immunostaining with zonula occludens-1 (ZO-1) antibody to visualize RPE cellular boundaries; loss of regular hexagonal cellular boundaries is indicative of degenerated RPE. (**f**) Immunoblots of pro-caspase-1 (pro-Casp1) and the p20 cleavage product of caspase-1 (Casp1 p20) in RPE tissue of WT and $Casp11^{-/-}$ mice injected subretinally with vehicle (Vehi) or *Alu* RNA. *n* = 3 mice per group. (**g**) Immunoblots of pro-caspase-1 and the p20 cleavage product of caspase-1 in WT and $Casp11^{-/-}$ mouse RPE cells treated with *Alu* RNA. (**h**) IL-18 secretion by WT and $Casp11^{-/-}$ mouse RPE cell*s* mock transfected or transfected with *Alu* RNA. *n* = 3 independent experiments. Data presented are mean ± SD; $^{*}P = 0.014$, two-tailed t test. (**i**) Top, fundus photographs of the retinas of WT (n = 8 eyes), caspase-1 and caspase-11 deficient (n = 7 eyes) mice ($Casp1^{-/-}$ $Casp11^{129mt/129mt}$) as well as $Casp1^{-/-}$ $Casp11^{129mt/129mt}$ (n = 8 eyes) mice expressing functional mouse caspase-11 from a bacterial artificial chromosome transgene ($Casp1^{-/-}$ $Casp11^{129mt/129mt}$ $Casp11^{Tg}$) subretinally injected with vehicle or *Alu* RNA. For all immunoblots, cropped gel image of bands of interest of representative immunoblots of three independent experiments and densitometric analysis (mean (SEM)) are shown. Tubulin or β-actin or Vinculin was as a loading control as indicated in each blot. In **d**, **e** and **i**, binary (Healthy %) and morphometric quantification (PM, polymegethism (mean (SEM))) of RPE degeneration are shown (Fisher's exact test for binary; two-tailed t test for morphometry; $^{*}P < 0.05$; $^{**}P < 0.01$; $^{***}P < 0.001$). The degenerated retinal area is outlined by blue arrowheads in the fundus images. Loss of regular hexagonal cellular boundaries in ZO-1 stained flat mounts is indicative of degenerated RPE.

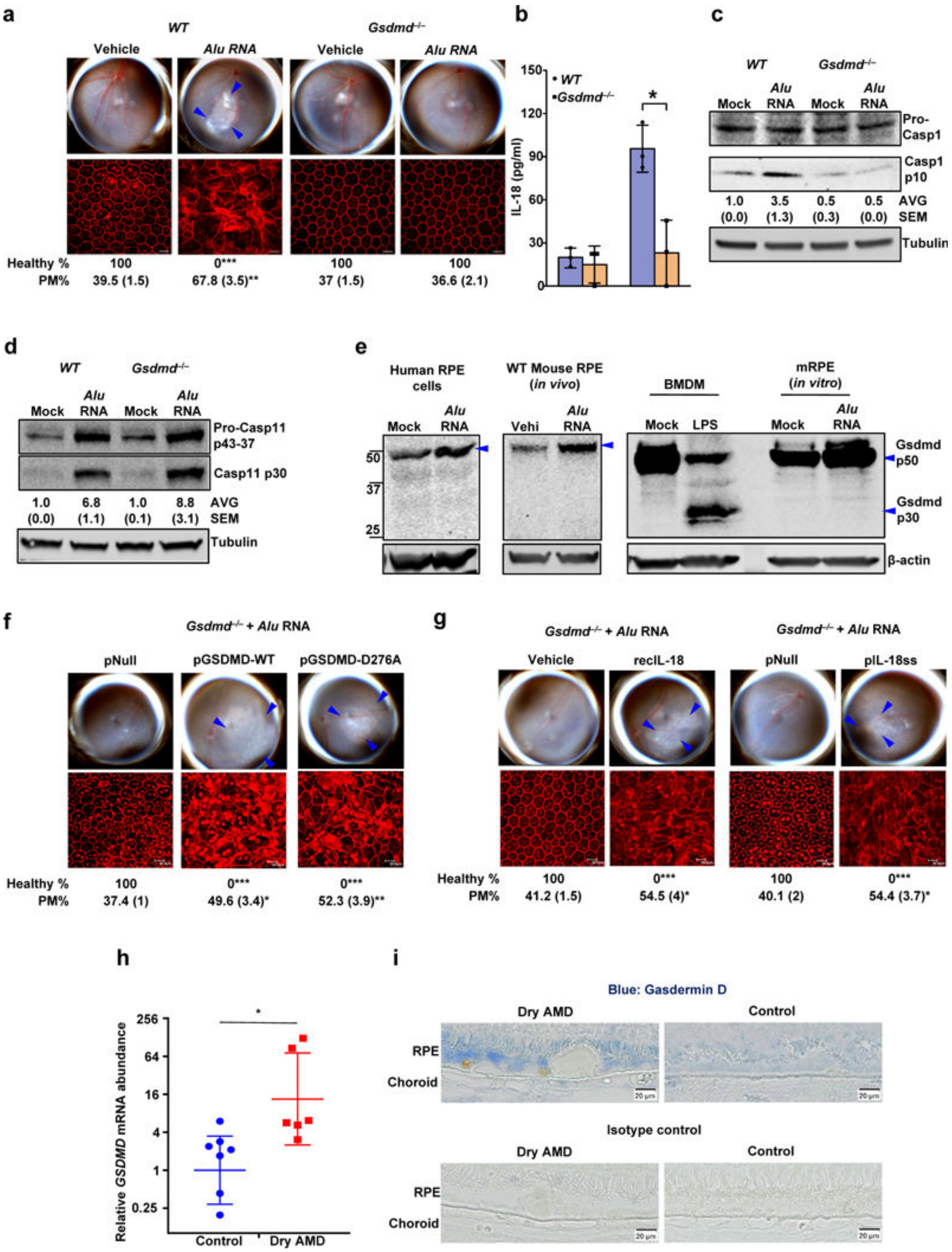

Figure 2. Gasdermin D in geographic atrophy and RPE degeneration

(**a**) Top, fundus photographs of eyes of WT (n = 6 eyes), and *Gsdmd*$^{-/-}$ (n = 10 eyes) mice subretinally injected with vehicle or *Alu* RNA. Bottom, immunofluorescence staining of zonula occludens-1 (ZO-1) on RPE flat mounts of the same eyes showing RPE cell boundaries. (**b**) IL-18 secretion by WT and *Gsdmd*$^{-/-}$ mouse RPE cell*s* mock transfected or transfected with *Alu* RNA (n = 3 independent experiments; Data presented are mean ± SD, **P* = 0.01, two-tailed t test) (**c**) Immunoblots of pro-caspase-1 (pro-Casp1) and the p10 cleavage product of caspase-1 (Casp1 p10) in WT and *Gsdmd*$^{-/-}$ mouse RPE cells mock transfected or transfected with *Alu* RNA. (**d**) Immunoblots of pro-caspase-11 (pro-Casp11) and the p30 cleavage product of caspase-11 (Casp11 p30) in WT and *Gsdmd*$^{-/-}$ mouse RPE cells mock transfected or transfected with *Alu* RNA. (**e**) Immunoblots of Gasdermin D and cleavage product of Gasdermin D (Gsdmd p30) in mock transfected or *Alu* RNA transfected human primary RPE cells, WT mouse primary RPE cells, and WT BMDM as well as in RPE tissue from WT mice subretinally injected with vehicle or *Alu* RNA. (**f**, **g**) Fundus photographs and immunofluorescence staining of zonula occludens-1 (ZO-1) on RPE flat mounts, (**f**) *Gsdmd*$^{-/-}$ mice reconstituted via *in vivo* subretinal transfection of empty vector plasmid (pNull; n = 4 eyes), plasmids expressing wild type gasdermin D (pGSDMD-WT; n = 4 eyes) or mutant gasdermin D incapable of undergoing p30 cleavage (pGSDMD-D276A; n = 5 eyes) subretinally injected with *Alu* RNA. (**g**) *Gsdmd*$^{-/-}$ mice subretinally administered vehicle control (Vehicle; n = 4 eyes), recombinant mature IL-18 (recIL-18; n = 4 eyes), mature IL-18 expression plasmid (pIL-18ss; n = 5 eyes) or empty vector control (pNull; n = 4 eyes) were subretinally injected with *Alu* RNA. (**h**) RT-qPCR examination of *GSDMD* mRNA abundance in the RPE tissue of human AMD eyes (n = 7 eyes) and in healthy age-matched control eyes ($n = 6$ eyes). $^{*}P = 0.045$, two-tailed t test; error bars denote geometric means with 95% confidence intervals. (**i**) Immunolocalization of gasdermin D in the RPE of human geographic atrophy eyes and age-matched healthy controls. For all immunoblots, cropped gel image of bands of interest of representative immunoblots of three independent experiments and densitometric analysis (mean (SEM)) are shown. In **a**, **f** and **g**, binary (Healthy %) and morphometric (PM, polymegethism (mean (SEM)) quantification of RPE degeneration are shown (Fisher's exact test for binary; two-tailed t test for morphometry; $^{*}P < 0.05$; $^{**}P < 0.01$; $^{***}P < 0.001$). Loss of regular hexagonal cellular boundaries in ZO-1 stained flat mounts is indicative of degenerated RPE. The degenerated retinal area is outlined by blue arrowheads in the fundus images.

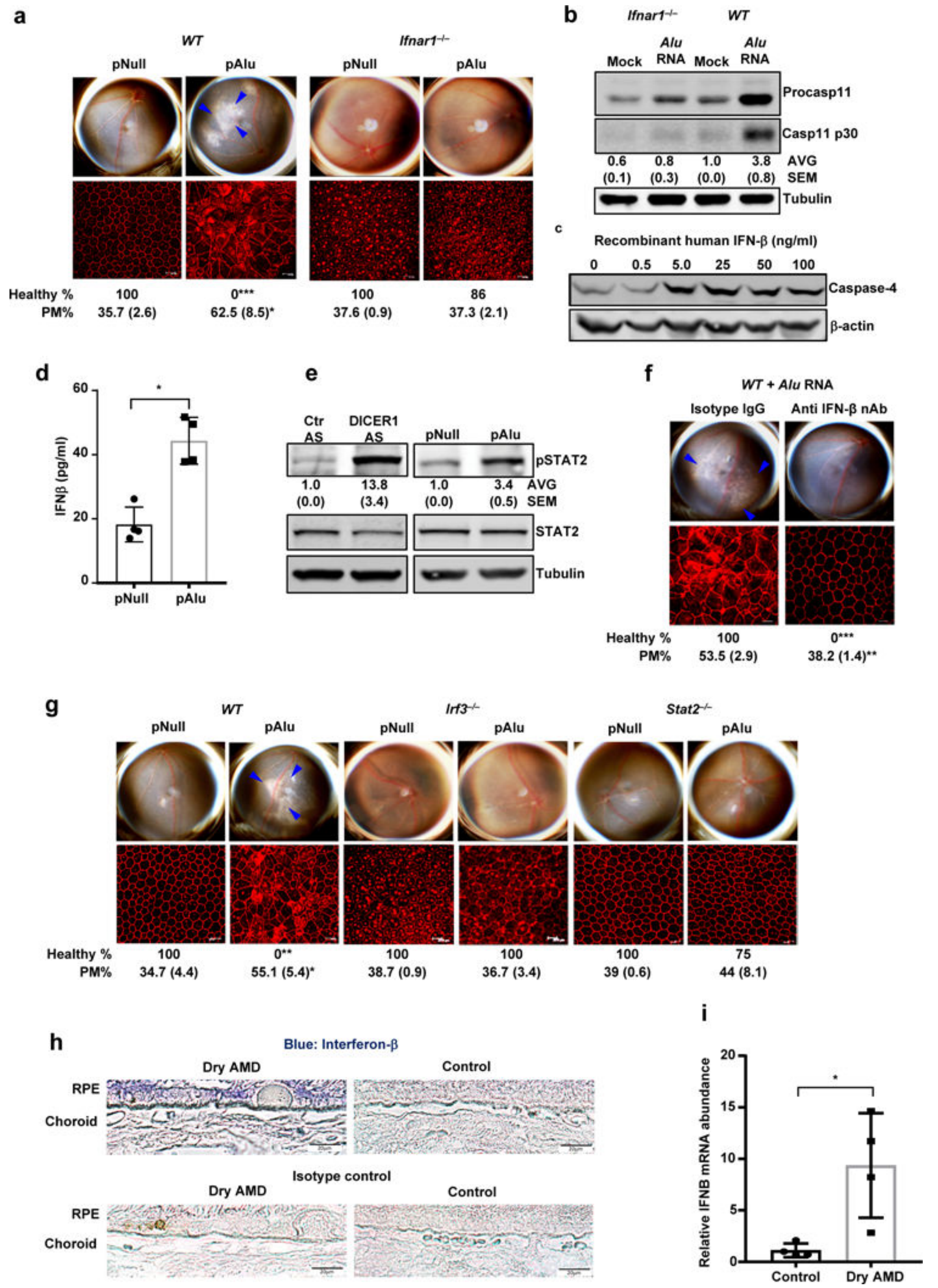

Figure 3. Non-canonical inflammasome activation and RPE degeneration induced by *Alu* RNA is mediated by interferon signaling

(**a**) Top, fundus photographs of eyes of WT (n = 7 eyes) and *Ifnar*$^{-/-}$ (n = 14 eyes) mice subretinally injected with *Alu* expression plasmid (pAlu) or empty vector (pNull). Bottom, immunofluorescence staining of zonula occludens-1 (ZO-1) on RPE flat mounts of the above eyes showing RPE cell boundaries. (**b**) Immunoblot of pro-caspase-11 (pro-Casp1) and the p30 cleavage product of caspase-11 (Casp11 p30) in WT and *Ifnar*$^{-/-}$ mouse RPE cells mock transfected or transfected with *Alu* RNA. (**c**) Immunoblot of pro-caspase-4 in

IFN-β-treated human RPE cells. (**d**) IFN-β secretion by human RPE cells transfected with *Alu* expression plasmid (pAlu) or empty vector (pNull). Data presented are mean ± SD; n = 3 independent experiments; $^*P = 0.0012$, two-tailed t test. (**e**) Immunoblot of phosphorylated STAT2 (pSTAT2) and total STAT2 in human RPE cells transfected with *Alu* expression plasmid (pAlu) or empty vector (pNull) or DICER1 or control (Ctr) anti-sense oligonucleotides (AS). (**f**) Fundus photographs and immunofluorescence staining of zonula occludens-1 (ZO-1) on RPE flat mounts of WT mice subject to *Alu* RNA co-administration with IFN-β neutralizing antibody (n = 6 eyes) or Isotype IgG (n = 4 eyes). (**g**) Fundus photographs and immunofluorescence staining of zonula occludens-1 (ZO-1) on RPE flat mounts of WT (n = 6 eyes) or $Irf3^{-/-}$ (n = 6 eyes) or $Stat2^{-/-}$ (n = 7 eyes) mice subretinally injected with *Alu* expression plasmid (pAlu) or empty vector (pNull). (**h**) Immunolocalization of IFN-β in the RPE of human geographic atrophy eyes and age-matched unaffected controls. Representative image from control and Dry AMD eyes are presented, n = 4 eyes. (**i**) Abundance of IFN-β mRNA in the RPE of the human geographic atrophy eyes compared to age-matched healthy controls, (Data presented are mean ± SEM; n = 4 eyes; $^*P = 0.018$, two-tailed t test). For all immunoblots, cropped gel image of bands of interest of representative immunoblots of three independent experiments and densitometric analysis (mean (SEM)) are shown. In **a**, **f** and **g**, binary (Healthy %) and morphometric (PM, polymegethism (mean (SEM)) quantification of RPE degeneration are shown (Fisher's exact test for binary; two-tailed t test for morphometry; $^*P < 0.05$; $^{**}P < 0.01$; $^{***}P < 0.001$). Loss of regular hexagonal cellular boundaries in ZO-1 stained flat mounts is indicative of degenerated RPE. The degenerated retinal area is outlined by blue arrowheads in the fundus images.

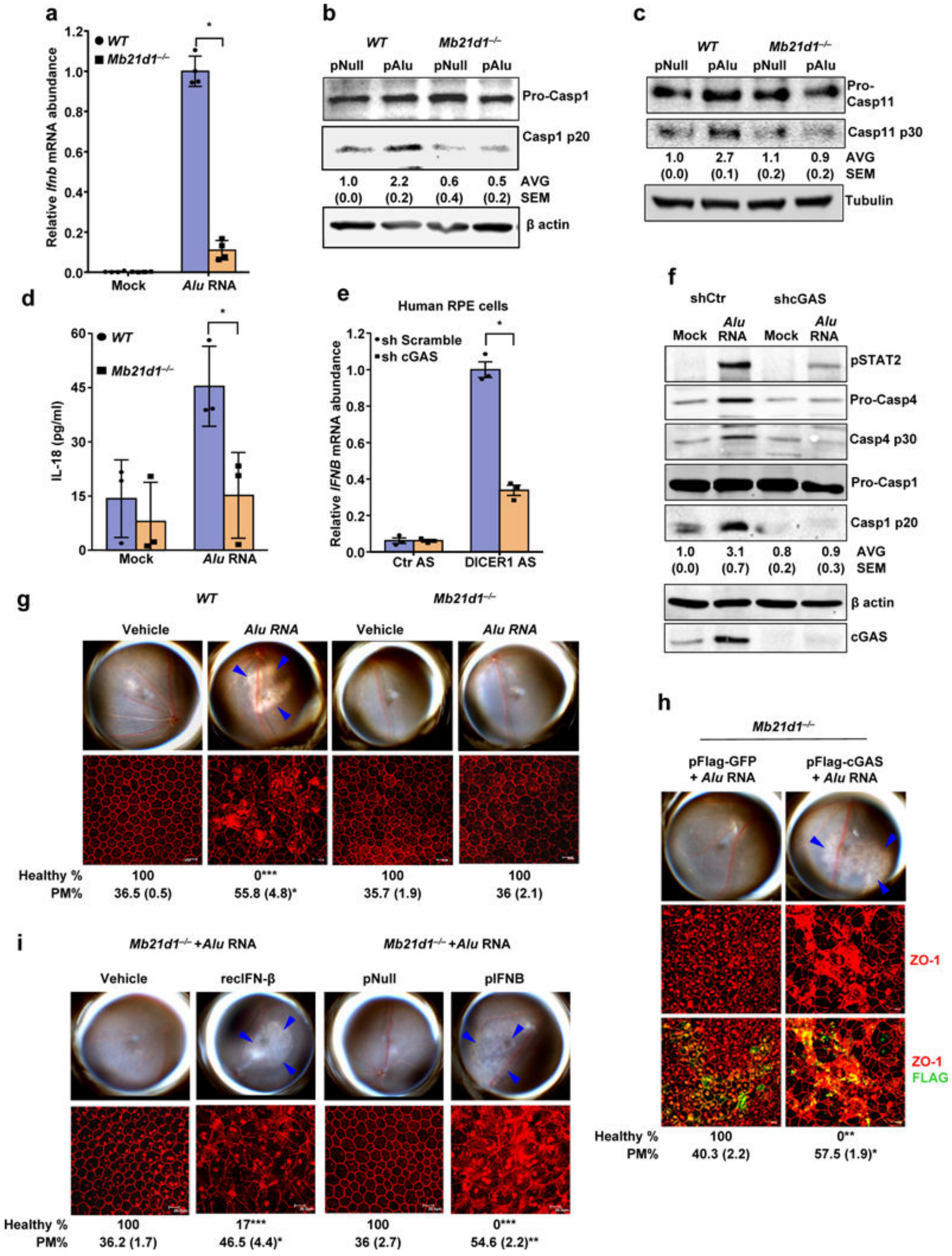

Figure 4. cGAS driven signaling licenses non-canonical inflammasome and RPE degeneration

(**a**) Relative abundance of *Ifnb* mRNA in WT and *Mb21d1*$^{-/-}$ mouse RPE cells mock-transfected or transfected with *Alu* RNA. Data presented are mean ± SEM; *n* = 4 cell culture replicates; **P* = 0.0001, two-tailed t test. (**b**) Immunoblots of pro-caspase-1 (pro-Casp1) and the p20 cleavage product of caspase-1 (Casp1 p20) in WT and *Mb21d1*$^{-/-}$ mouse RPE cells transfected with *Alu* expression plasmid (pAlu) or empty vector control (pNull). (**c**) Immunoblots of pro-caspase-11 (pro-Casp1) and the p30 cleavage product of caspase-1 (Casp11 p30) in WT and *Mb21d1*$^{-/-}$ mouse RPE cells transfected with *Alu* expression plasmid (pAlu) or empty vector control (pNull). (**d**) IL-18 secretion by WT and *Mb21d1*$^{-/-}$ mouse RPE cells mock transfected or transfected with *Alu* RNA. Data presented are mean ± SD; $n = 3$ independent experiments; $^*P = 0.032$, two-tailed t test. (**e**) Relative abundance of *IFNB* mRNA in control (sh Scramble) or cGAS shRNA knockdown human RPE cells transfected with or DICER1 or control (Ctr) anti-sense oligonucleotides (AS). Data presented are mean ± SEM; $n = 3$ cell culture replicates; $^*P = 0.0002$, two-tailed t test. (**f**) Immunoblot of phosphorylated STAT2 (pSTAT2); pro-caspase-4 and casp4 p30; pro-caspase-1 and p20 cleavage casp1 p20 in control (sh Scramble) or cGAS shRNA knockdown human RPE cells mock-transfected or transfected with *Alu* RNA. Knockdown efficiency of cGAS is shown by cGAS immunoblot and tubulin was used as a loading control. (**g**) Fundus photographs and immunofluorescence staining of zonula occludens-1 (ZO-1) on RPE flat mounts of WT (n = 6 eyes) and *Mb21d1*$^{-/-}$ (n = 8 eyes) mice subretinally injected with vehicle or *Alu* RNA. (**h**) Fundus photographs and immunofluorescence staining of zonula occludens-1 (ZO-1) on RPE flat mounts of *Mb21d1*$^{-/-}$ (n = 7 eyes) mice reconstituted by in vivo transfection of cGAS expression plasmid (pFlag-cGAS) or control GFP expression plasmid (pFlag-GFP), subretinally injected with *Alu* RNA. (**i**) Fundus photographs and immunofluorescence staining of zonula occludens-1 (ZO-1) on RPE flat mounts of *Mb21d1*$^{-/-}$ mice subretinally co-administered *Alu* RNA with recombinant IFN-β (n = 6 eyes), vehicle control (n = 6 eyes), IFN-β expression plasmid (pIFNB; n = 5 eyes) or empty vector control (pNull; n = 5 eyes). For all immunoblots, cropped gel image of bands of interest of representative immunoblots of three independent experiments and densitometric analysis (mean (SEM)) are shown. In **g**, **h** and **i**, binary (Healthy %) and morphometric (PM, polymegethism (mean (SEM)) quantification of RPE degeneration are shown (Fisher's exact test for binary; two-tailed t test for morphometry; $^*P < 0.05$; $^{**}P < 0.01$; $^{***}P < 0.001$). Loss of regular hexagonal cellular boundaries in ZO-1 stained flat mounts is indicative of degenerated RPE. The degenerated retinal area is outlined by blue arrowheads in the fundus images.

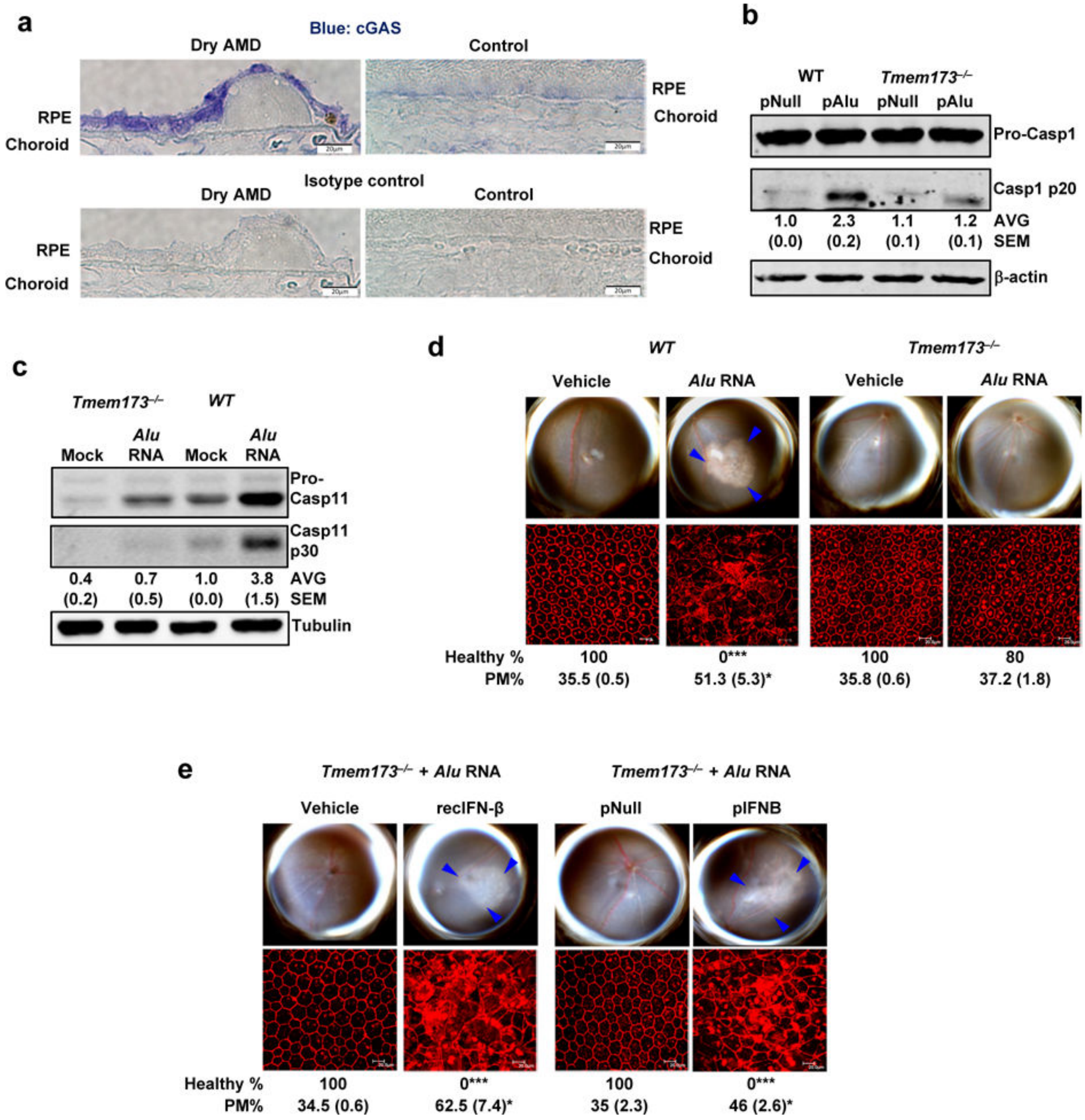

Figure 5. cGAS in geographic atrophy and RPE degeneration

(**a**) Immunolocalization of cGAS in the RPE of human geographic atrophy eyes and age-matched unaffected controls. Representative image from control and Dry AMD eyes are presented, n = 4 eyes. (**b**) Immunoblots of pro-caspase-1 and p20 cleavage product of caspase-1 (Casp1 p20) in *WT* and *Tmem173*$^{-/-}$ mouse RPE cells transfected with *Alu* expression plasmid (pAlu) or empty vector control plasmid (pNull). (**c**) Immunoblots of pro-caspase-11 and p30 cleavage product of caspase-11 (Casp11 p30) in WT and *Tmem173*$^{-/-}$ mouse RPE cells mock transfected or transfected with *Alu* RNA. (**d**) Fundus photographs and immunofluorescence staining of zonula occludens-1 (ZO-1) on RPE flat mounts of WT (n = 6 eyes) and *Tmem173*$^{-/-}$ (n = 10 eyes) mice subretinally injected with vehicle or *Alu* RNA. (**e**) Fundus photographs and immunofluorescence staining of zonula occludens-1

(ZO-1) on RPE flat mounts of *Tmem173*$^{-/-}$ mice subretinally co-administered *Alu* RNA with recombinant IFN-β (n = 4 eyes) or vehicle control (n = 4 eyes); or IFN-β expression plasmid (pIFNB; n = 4 eyes) or empty vector control (pNull; n = 4 eyes). For all immunoblots, cropped gel image of bands of interest of representative immunoblots of three independent experiments and densitometric analysis (mean (SEM)) are shown. In **d** and **e**, binary (Healthy %) and morphometric (PM, polymegethism (mean (SEM)) quantification of RPE degeneration are shown (Fisher's exact test for binary; two-tailed t test for morphometry; $*P < 0.05$; $**P < 0.01$; $***P < 0.001$). Loss of regular hexagonal cellular boundaries in ZO-1 stained flat mounts is indicative of degenerated RPE. The degenerated retinal area is outlined by blue arrowheads in the fundus images.

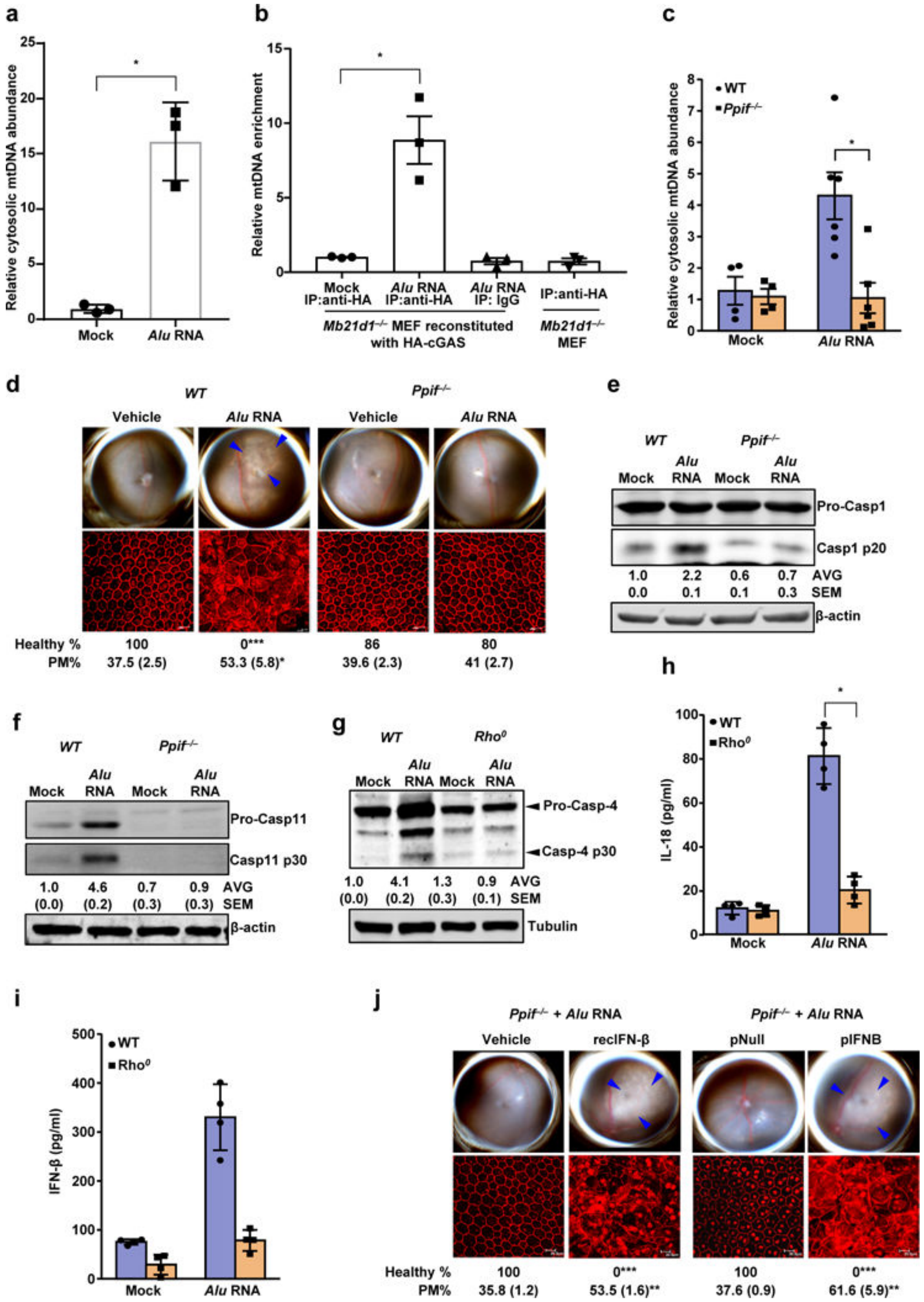

Figure 6. mtDNA in non-canonical inflammasome activation and RPE degeneration

(**a**) Relative abundance of cytosolic mitochondrial DNA (mtDNA) in human RPE cells mock-transfected or transfected with *Alu* RNA (Data presented are mean ± SEM; n = 3 independent experiments; *P = 0.0018, two-tailed t test). (**b**) Relative enrichment of mtDNA in cGAS immunoprecipitate in ChIP like pull-down assay. Mock or *Alu* RNA transfected, indicated mouse embryonic fibroblast (MEF) were analyzed upon HA-cGAS immunoprecipitation with anti-HA antibody or isotype conrol. Data presented are mean ± SEM; n = 3; *P = 0.008, two-tailed t test. (**c**) Relative abundance of cytosolic mitochondrial

DNA (mtDNA) in WT and *Ppif*$^{-/-}$ mouse RPE cells mock transfected (n = 4 cell culture replicates) or transfected with *Alu* RNA (Data presented are mean ± SEM; n = 6 cell culture replicates; $^*P = 0.004$, two-tailed t test). (**d**) Fundus photographs and immunofluorescence staining of zonula occludens-1 (ZO-1) on RPE flat mounts of WT (n = 6 eyes) and *Ppif*$^{-/-}$ (n = 12 eyes) mice subretinally injected with vehicle or *Alu* RNA. (**e**) Immunoblot for procaspase-1 (procasp-1) and p20 cleavage product of caspase-1 in WT and *Ppif*$^{-/-}$ mouse RPE cells mock transfected or transfected with *Alu* RNA. (**f**) Immunoblot for procaspase-11 (procasp-11) and p30 cleavage product of caspase-11 (Casp11 p30) in WT and *Ppif*$^{-/-}$ mouse RPE cells mock transfected or transfected with *Alu* RNA. (**g**) Immunoblot for procaspase-4 (procasp-4) and p30 cleavage product of caspase-4 (Casp4 p30) in WT and mitochondrial DNA deficient *Rho*^{0} ARPE19 human RPE cells mock-transfected or transfected with *Alu* RNA. (**h**, **i**) WT and mitochondrial DNA deficient *Rho*^{0} ARPE19 human RPE cells mock-transfected or transfected with *Alu* RNA. (h) IL-18 secretion; data presented are mean ± SD; n = 4 independent experiments; $^*P = 0.0001$, two-tailed t test. (**i**) IFN- β secretion; data presented are mean ± SD; n = 4 independent experiments; $^*P = 0.004$, two-tailed t test. (**j**) Fundus photographs and immunofluorescence staining of zonula occludens-1 (ZO-1) on RPE flat mounts of the *Ppif*$^{-/-}$ mice subretinally co-administered *Alu* RNA with recombinant IFN-β (n = 5 eyes) or vehicle control (n = 5 eyes); or IFN-β expression plasmid (pIFNB; n = 6 eyes) or empty vector control (pNull; n = 5 eyes). For all immunoblots, cropped gel image of bands of interest of representative immunoblots of three independent experiments and densitometric analysis (mean (SEM)) are shown. In **d** and **j**, binary (Healthy %) and morphometric (PM, polymegethism (mean (SEM)) quantification of RPE degeneration are shown (Fisher's exact test for binary; two-tailed t test for morphometry; $^*P < 0.05$; $^{**}P < 0.01$; $^{***}P < 0.001$). Loss of regular hexagonal cellular boundaries in ZO-1 stained flat mounts is indicative of degenerated RPE. The degenerated retinal area is outlined by blue arrowheads in the fundus images.